Revista Científica Periódica Volume 07 - Número 02 - Dezembro de 2004

ISSN 1516-2338

TELECOMUNICAÇÕES

Inatel

Revista do Instituto Nacional de Telecomunicações

Editorial

Tutorial

Artigos

Revista Científica/Periódica publicada pelo Inatel - Instituto Nacional de Telecomunicações

Diretor: Wander Wilson Chaves
Vice-diretor: Carlos Roberto dos Santos

Expediente

Assessoria de Comunicação & Marketing - ASCOM
e-mail: ascom@inatel.br

Diagramação
Centro de Informações Científicas e Tecnológicas
Setor de Editoração Eletrônica

Tiragem: 5.300 exemplares
Distribuição Gratuita

Instituto Nacional de Telecomunicações
Av. João de Camargo, 510
Caixa Postal: 05
Santa Rita do Sapucaí - MG - BRASIL
CEP 37540-000
Tel: (35) 3471.9200 Fax: (35) 3471.9314
e-mail: inatel@inatel.br
http://www.inatel.br

EDITORIAL

Este número da revista *Telecomunicações* apresenta uma excelente seleção de trabalhos científicos de pesquisadores de renomadas instituições. Em primeiro lugar, em artigo convidado, Strobel faz uma apresentação geral dos sistemas de comunicações ópticas e das propriedades dos componentes mais importantes a elas associados. São destacadas as conquistas mais modernas que permitiram o desenvolvimento de modelos para elevadas taxas de transmissão, com previsões superiores a 40Gbit/s. Um segundo artigo descreve o método das diferenças finitas no domínio da freqüência aplicado a estruturas periódicas bidimensionais com anisotropia biaxial. O objetivo principal do trabalho é estabelecer a dependência entre as características geométricas da estrutura e as propriedades de propagação da onda eletromagnética guiada no modo TM.

Nos últimos anos, tem crescido de forma marcante o interesse por dispositivos envolvendo tecnologias de óptica integrada. Dentro dessa visão, incontáveis progressos foram feitos em componentes passivos e ativos para a compactação de sistemas e subsistemas ópticos. Os moduladores eletroópticos externos, capazes de suplantar os modelos de modulação direta em diversos aspectos, sofreram rápida evolução e têm garantido a possibilidade de taxas de transmissão cada vez mais elevadas. Este assunto representa o núcleo do terceiro artigo, que é a análise de um modulador eletroóptico de niobato de lítio baseado no interferômetro de Mach-Zehnder. A abordagem é feita por meio do método dos elementos finitos e o comportamento do dispositivo é analisado para um substrato com corte *x*. Apresentam-se os efeitos de alguns parâmetros de fabricação do guia óptico sobre a eficiência global do modulador e sobre sua resposta em freqüência.

Dentro da mesma perspectiva do artigo anterior, Franco *et al*. exploram a construção de eletrodos apoiados sobre uma camada isolante de dóxido de silício em moduladores integrados. A análise matemática utiliza o método dos elementos finitos aplicado também a um modulador com interferômetro de Mach-Zehnder com os eletrodos sobre um substrato de niobato de lítio com corte em *x*. Os autores comparam os resultados da estrutura analisada com os oriundos de outros modelos já conhecidos. Fica evidente o aumento na largura de faixa do sinal de modulação e a redução no consumo de potência em relação aos modelos convencionais.

Um projeto acadêmico que inclua a publicação periódica de uma revista científica exige a colaboração de muitas pessoas, entidades e empresas. Este fato tem sido uma constante no caso da revista *Telecomunicações* e neste número pôde-se contar com o apoio da empresa ***Advanstar***, organizadora há anos do tradicional evento Telexpo. Fica aqui registrado o reconhecimento de toda a equipe editorial. Devem ser reconhecidas, com igual ênfase, as inestimáveis participações dos autores, com artigos de elevado padrão, que têm garantido o sucesso do empreendimento nos meios técnicos e acadêmicos do país. Estas colaborações serão sempre bem vindas e de importância fundamental para garantir a continuidade da publicação.

Prof. José Antônio Justino Ribeiro
Convidado pelo Editor

Fiber-Optic Transmission – an Overview

Otto A. Strobel

Department of Basic Sciences - Esslingen University of Applied Sciences
73732 Esslingen, Germany

Invited Paper

***Abstract* – The idea of this paper is to give an overview on fiber-optic communication. The most important devices for fiber-optic transmission systems are presented, and their properties discussed. In particular we consider such systems working with those basic components which are necessary to explain the principle of operation. Among them is the optical transmitter, consisting of a light source, typically a high speed driven laser diode. Furthermore, the optical receiver has to be mentioned; it consists of a photodiode and a low noise high bit rate front-end amplifier. Yet, in the focus of the considerations you will find the optical fiber as the dominant element in optical communication systems. Different fiber types are presented, and their properties explained. The joint action of these three basic components leads to fiber- optic systems, mainly applied for data communication. The systems operate as transmission links with bit rates up to 40 Gbit/s.**

I. INTRODUCTION

Since the beginning of the sixties, there has been a light source which yields a completely different behavior compared to the sources we had before: This light source is the LASER. The first realized laser was the bulk-optic ruby laser [1]. Short time after this very important achievement, diode lasers for use as optical transmitters have already been developed (see Fig.1) [2]. Parallel to that accomplishment in the early seventies, researchers and engineers accomplished the first optical glass fiber with sufficient low attenuation to transmit electromagnetic waves in the near infrared region [3].

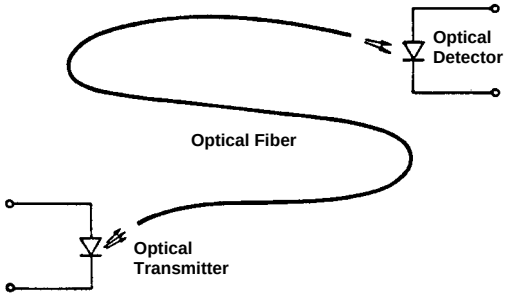

Figure 1 – Basic arrangement of a fiber-optic system.

The photodiode as detector already worked [4], and thus, systems could be developed using optoelectric (O/E) and electrooptic (E/O) components for transmitters and receivers as well as a fiber in the center of the arrangement. The main fields of application of such systems are found in the area of fiber-optic transmission and fiber-optic sensors (see Fig.2).

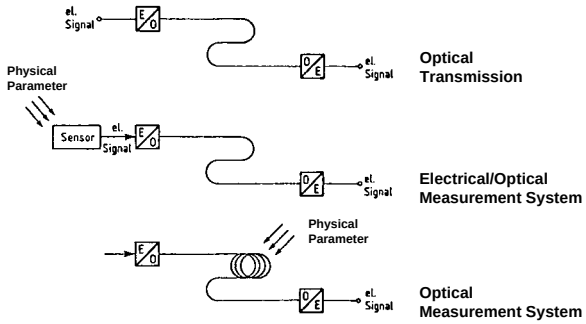

Figure 2 – Application of fiber-optic systems.

However, the first optical transmission is much older. Indians for instance, had already communication by smoke signals long time ago (see Fig.3, [5]). Furthermore, it was a very sophisticated and modern system, because it was already a digital system, consisting of "binary 1" and "binary 0" (smoke/no smoke).

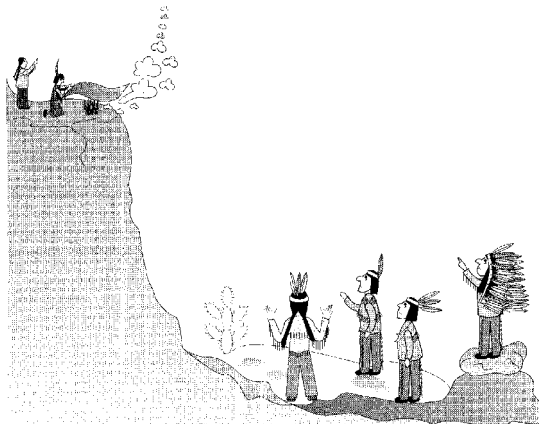

Figure 3 – Digital optical transmission by use of smoke signals.

As inventors of fiber-optic transmission systems can be regarded Charles Kao (1963, [6]) and Manfred Börner (1964, [7]). Nowadays, their invention would not be very spectacular: Take a light source as transmitter, an optical fiber as transmission medium, and a photodiode as detector (see Fig.1)! Yet, in 1963, it was a revolution, because the attenuation of optical glass was in the order of 1000 dB/km, and therefore totally unrealistic for use in practical systems. Today's fibers achieve an attenuation below 0.2 dB/km which means otherwise that after 100 km, there is still more than 1% of light at the end of the fiber. This low value of attenuation is one of the most attractive advantages of fiber-optic systems, compared to

conventional electrical ones (see Fig.4). In addition, low weight, small size, insensitivity against electromagnetic interference (EMI), electrical insulation and low crosstalk must be mentioned. Apart from low attenuation, the enormous achievable bandwidth must be pointed out. That leads to a high transmission capacity in terms of the product of fiber bandwidth and length. One of the most important goals is to maximize this product for every kind of data transmission. Figure 4 depicts the attenuation behavior. In particular we observe an independence on modulation frequency of fiber-optic systems in contrast to electrical ones which suffer from the skin effect.

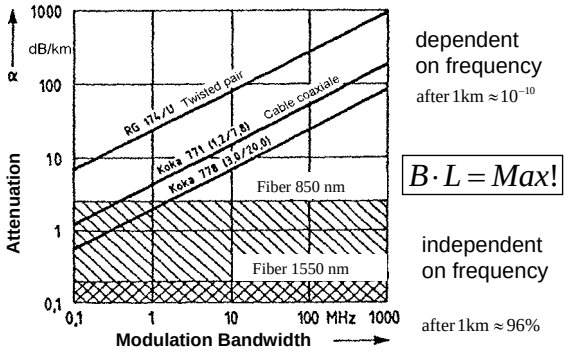

Figure 4 – Attenuation of coaxial cables and optical fibers.

II. OPTICAL FIBERS

Most important demands on optical fibers are a proper waveguiding, low loss of optical power and low distortion of the transmitted optical signals. The principle of operation of guiding a light wave can be explained by Snell's law (see Fig.5). If light is incident on an interface between two media with different refraction indices (n_1 and n_2) in general there is a reflected and a refracted ray. But for the special case that light is incident from a media

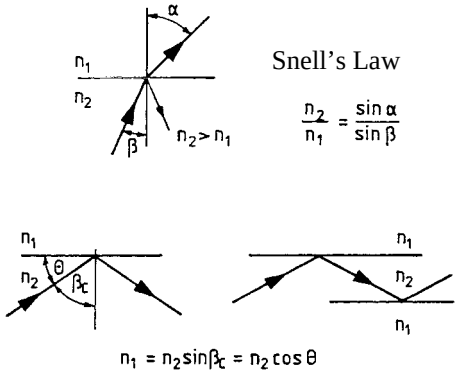

Figure 5 – Refraction, reflection and total internal reflection for light transition between two different media.

with higher refraction index ($n_2 > n_1$) as compared to the following one and furthermore the angle β exceeds a certain value (the cut-off angle β_c) there is no refraction anymore. We get reflection exclusively, the whole light is totally reflected; this effect is called "total internal reflection".

If this total internal reflection is repeated at a second interface a waveguide is achieved [8]. Figure 6 depicts this behavior. In particular it has to be pointed out that there is no loss due to the multiple reflection because it is a total internal reflection; the coefficient $R = 1$ holds for every repeated reflection. Thus, the attenuation of the fiber is only due to losses inside the fiber.

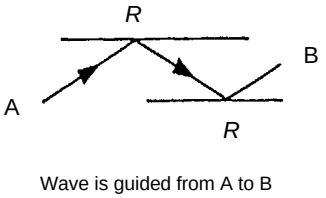

Figure 6 – Total internal refraction and waveguiding.

The most important attenuation mechanisms are Rayleigh scattering and OH^- absorption. The scattering effect is due to inhomogeneities in the molecular structure of glass (silicon dioxide: SiO_2). Hence, statistical refraction index changes are caused. This leads to a scattering effect of the traveling light wave in the fiber, causing loss. The loss strongly depends on the wavelength of the light wave (scattered power P_S, see Fig.19). Lord Rayleigh discovered and explained that due to this effect the color of the sky is blue. When we look at the sky, we see the scattered light of the white sunlight. Blue light is much more scattered than red. The same reason causes much higher losses in glass fibers for blue light than for red one (see Fig.19). Therefore, fiber-optic systems operate even beyond the red area, in the infrared (see below).

Figure 19 depicts also high attenuation peaks. These peaks are due to light absorption at undesired molecules in glass. The most important enemy in a fiber is water which appears as OH^- ions in the silicon dioxide structure. The OH^-molecules are brought to oscillations by light waves. This effect is in particular dominant when resonance occurs at wavelengths which fit (see peaks). Hence, the energy of a light wave traveling in the fiber is absorbed, which leads to high attenuation. To achieve low fiber attenuation, the demand of purity is very high, the OH^- concentration must not exceed a value of 1 ppb. This was one of the reasons why it took a long time from the first idea of fiber transmission, in about 1963, to the first produced fiber in about 1972. Furthermore has to be mentioned that the fiber also suffers from SiO_2-self absorption in the ultraviolet (UV) and infrared (IR) region, which in principle cannot be avoided. Whereas the UV-absorption can be neglected compared to the much higher value caused by Rayleigh scattering, the IR-absorption is responsible for the attenuation rise beyond 1600 nm (see Fig.19).

Besides the attenuation, there is a second cardinal problem concerning data transmission in optical fibers. Light rays in the fiber are not only traveling under one single angle. Figure 7 shows three representative existing rays (among hundreds or thousands). The existing rays are called "modes" in fibers. It is obvious that they do have different geometrical path lengths L. Yet, the determining effect for data transmission is not the geometrical but the optical path length $g = nL$, the product of the refraction index and the geometrical path length L. However, this optical path length differs for the three

mentioned modes, too, because the refraction index in the fiber core is constant.

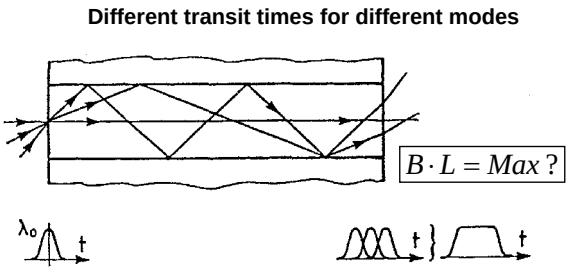

Figure 7 – Pulse broadening by modal dispersion.

Therefore, an optical pulse travels along all the three paths in the fiber. The consequence of this is, that they have different transit times and reach the fiber end at different arrival times. The three pulses superimpose and thus, we receive a broader output pulse as compared to the narrow input pulse (see Fig.7), the effect is called "pulse broadening". This behavior causes serious consequences. Since, if we want to transmit a high data rate, we have to place the second input pulse immediately after the first one. As a result, the pulses at the end of the fiber will overlap in such a manner that both pulses cannot be separated any longer. To avoid the overlap, it is necessary to place the second pulse with a greater distance from the first one which reduces the achievable bandwidth *B*. The second opportunity is to reduce the fiber length *L*. Both measures derogate the transmission capacity, the product of fiber bandwidth and length, the most important goal of every data transmission.

To avoid (reduce) this problem, scientists invented the graded-index fiber (see Fig.8). In contrast to the above described fiber, called "step-index fiber", the refraction index is not any longer constant across the fiber [9]. The latter reveals a gradient behavior in the fiber core, whereas it still remains constant in the envelope, the cladding.

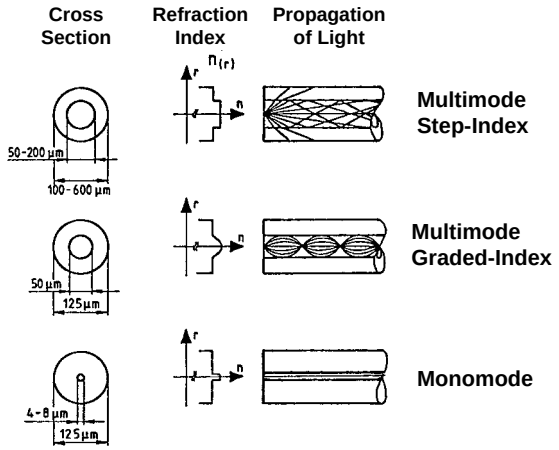

Figure 8 – Fiber types.

As a consequence, the optical path length $g = nL$ is now constant for each mode, because in the fiber center, one can remark the shortest geometrical path length *L* and the highest refraction index *n*. In contrast to this result near the cladding you find the longest geometrical path length linked with the lowest refraction index. Thus, with a properly chosen index profile we achieve a constant optical path length for all modes. At this stage, it has to be pointed out that it is not possible to achieve this goal completely, we obtain only a good approximation and thus there is still a certain modal dispersion left, resulting in a non negligible remain of transmission capacity reduction [10].

To overcome this problem, another invention was made, the construction of a monomode fiber: If we reduce the fiber core to a diameter below about ten micrometers, there will be only one ray, the ray along the optical axes transmitted and the modal dispersion problem vanishes per se [11]. For very high data rates (about 40 Gbit/s) we have to confess that this disappearance is not completely correct due to polarization effects. Very accurate investigations lead to the result that there is a difference between two perpendicularly oriented axes in the fiber concerning the refraction index. This fact again results in different optical path lengths, and finally as described before, in the same process of pulse broadening; this dispersion is called "polarization mode dispersion" (PMD [12]).

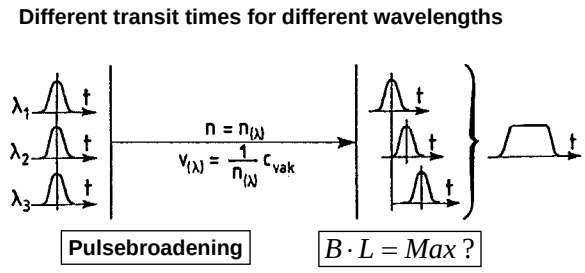

(*n*: Refraction Index, λ: Wavelength, c_{vak}: Free Space Velocity, *v*: Velocity in Media)

Figure 9 – Pulse broadening by material dispersion.

Furthermore, another important dispersion is to mention, the material dispersion [11]. Due to the fact that there is no light source emitting at a single wavelength (see Fig. 15), there is no monochromatic but always polychromatic light traveling through a fiber. Moreover, taking into account the dependence of the refraction index on the wavelength, it is obvious that we have always different refraction indices, and therefore, different optical path lengths according to different velocities of pulses traveling along the fiber.

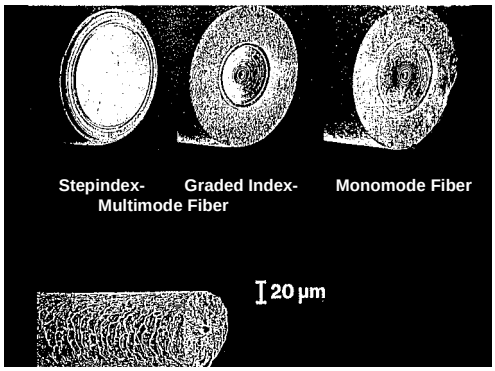

Figure 10 – Comparison of fiber types and a woman's hair.

Figure 9 shows three pulses having three representative wavelengths. They suffer from different transit times and reach the fiber end at different times of arrival. The three pulses superimpose as described above for the modal dispersion process and thus, we again

obtain a broader output pulse as compared to the narrow input pulse (see Fig.9). The result is the same as for modal dispersion, just the mechanism is different, the effect is again pulse broadening and reduction of the transmission capacity.

Figure 10 visualizes the three common fiber types in comparison with a woman's hair. Table 1 shows an overview on fiber types depicting most important fiber data. Furthermore, two more fiber types must be mentioned. There are also low cost applications concerning fiber-optic transmission, i.e. plastic fibers and PCS fibers (plastic cladding and silica core) are used, too. Their transmission capacity is much lower as compared to pure glass fibers in particular monomode fibers. However, there are applications for such fibers, e.g. if you have low data rates and only some ten meters of spacing. For example to watch a machine tool in an EMI relevant area, why not use a cheap plastic fiber transmission set-up in the kHz-region?

Type	Profile	Size	Attenuation	Bandwidth x Length
Plastic Fiber	Step Index	950/1000 µm	0,2 dB/m	< 100 MHz·m
PCS Fiber	Step Index	100 - 600 µm	6 dB/km	< 10 MHz·km
Multimode Glass	Step Index	> 100 µm	3 - 5 dB/km	20 MHz·km
Multimode Glass	Gradient Index	50/125 µm	2 dB/km (0.85 µm) 0,4 dB/km (1,3 µm) 0,2 dB/km (1,55 µm)	500 MHz·km
Monomode Glass		5 - 10 µm		> 100 GHz·km

Table 1 – Fiber types.

III. OPTICAL SOURCES AND DETECTORS

Most important demands on optical sources are a high optical output power as well as a small electrical input power. With regard to the fiber, the wavelengths should be in a proper range (see Fig.19). The spectral width has to be small, and for a sufficient coupling efficiency, the beam divergence should be low and the geometrical size should be small. Furthermore, a modulation capability of the injection current at high speed is favorable. To understand the principle of operation concerning optical sources and detectors, fundamental considerations about the interaction between photons and electrons have to be taken into account.

Figure 11 shows the energy band model of the semiconductor material, applied for the optical components. E_1 is the energy level of the valence band, whereas E_2 denotes the level of the conduction band. The difference ΔE between both levels is the energy gap E_g. There are three dominant effects to be considered:

A photon is incident onto the semiconductor material. Thereby, an electron is lifted from the valence to the conduction band followed by transportation in an external circuit if a voltage is applied. Thus, electric charge is moving, i.e. this is current which is generated, caused by the absorption of a photon. This is the desired behavior in a photodiode. The second effect goes the other way round, an electron transition from the conduction band to the valence band occurs spontaneously. The energy difference ΔE is converted into a photon. In particular, the process of a following electron transition causing a second photon has nothing to do with generation of the first photon, i.e. there is a statistical behavior, named "spontaneous emission". This process occurs in an LED [13]. In contrast to this process, the third one is completely different. The electron transition from conduction to valence band is not any longer a statistical process, but an induced or stimulated one. This process is stimulated by an already existing photon, e.g. produced by the spontaneous process. The two photons are not any longer strangers. They know each other, they are coherent, we receive a coherent radiation caused by stimulated emission. This is the desired behavior in a laser. The two photons, now and again, cause new transitions and multiply themselves. Thereby an avalanche is produced; we receive a large amplification after exceeding a certain threshold (see Fig.12), we receive a LASER: Light Amplification by Stimulated Emission of Radiation [14].

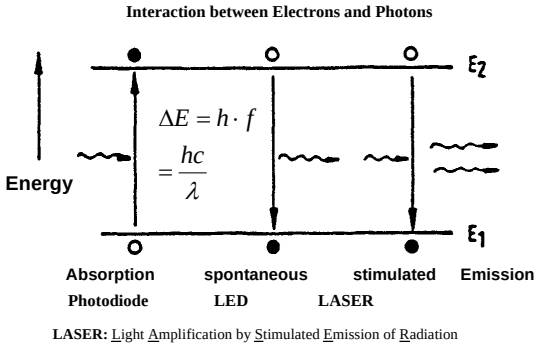

Figure 11 – Absorption and emission of photons.

Figure 12 depicts the optical power versus the injection current of a semiconductor laser. Below threshold the laser operates as an LED, after exceeding a certain injection current, the threshold current, stimulated emission takes place. Unfortunately there is a strong dependence of the threshold current on temperature. Hence, additional measures are necessary, such as temperature control or control by a monitor diode in order to stabilize the optical output power.

Figure 13 shows the far field distribution of a typical Fabry-Perot semiconductor laser. Unfortunately, semiconductor lasers show beam divergence and astigmatism, whereby the divergence is different in two perpendicular directions. Both effects make the coupling into a fiber in particular in a monomode fiber difficult. The laser chip is mounted up side down on a silicon substrate. This mounting enables a close contact of the active area to the heat sink. The chip size is about 300 µm long, 200 µm broad and 100 µm high, the active area is in the order of $1\mu m^2$. Figure 14 visualizes a comparison between LED and laser farfield. The LED is a Lambertian light source, and thus it emits the radiation in the half sphere which makes the fiber coupling even more difficult.

A further interesting comparison between laser and LED is concerned with coherence properties. Figure 15 shows that the spectral width of a laser diode is much smaller than that of an LED, i.e. the laser coherence length is much larger as compared to the LED.

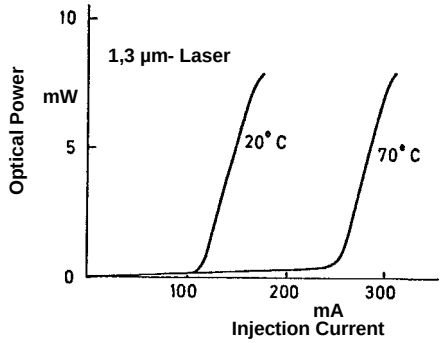

Figure 12 – Optical power versus injection current.

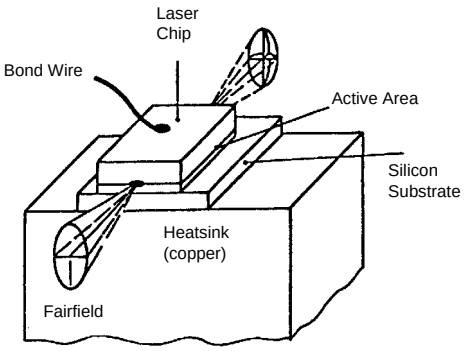

Figure 13 – Schematic arrangement of a semiconductor laser.

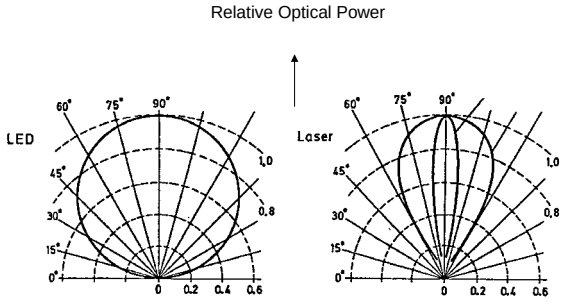

Figure 14 – Farfield characteristics of LED and Laser.

To depict both spectra in a single diagram, the laser power had to be reduced by a factor of 50. Moreover, it has to be mentioned that the 2 nm of laser width is just a rough idea. It could also be smaller by several decades. This results in a much better behavior concerning the material dispersion of a fiber. Thus, optical power, farfield behavior and spectral size enable the laser much more for highly sophisticated optical transmission systems, and hence for high speed long distance systems exclusively lasers are applied. In contrast to the laser, LEDs are used for low cost, low bit rate and low distance systems.

Most important demands on optical detectors [15, 16] are high sensitivity, low noise, linearity (for analog systems only) and small geometrical size. Most famous components are pin-photodiodes (see Fig. 16 and 17) and avalanche photodiodes (APDs). All photodiodes for transmission systems are used in reverse voltage operation. This operation applies an electric field to the semiconductor material and thus an electron produced by photon absorption is experiencing a force and will be accelerated. This effect is even enlarged by introducing an intrinsic zone into a pn-diode, which results in a pin-diode. This design guaranties a constant and high electric field over the whole absorption zone whereas the pn-diode has only a maximum directly at the pn-junction which leaves most part of the absorption area in a low electric field. Therefore the pin-diode is able to operate as a high speed component.

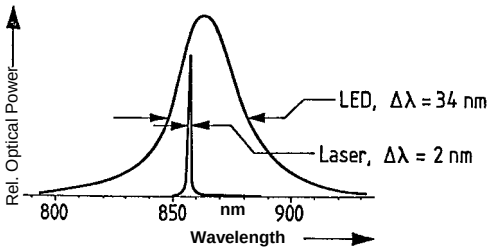

Figure 15 – Spectral width of LED and Laser.

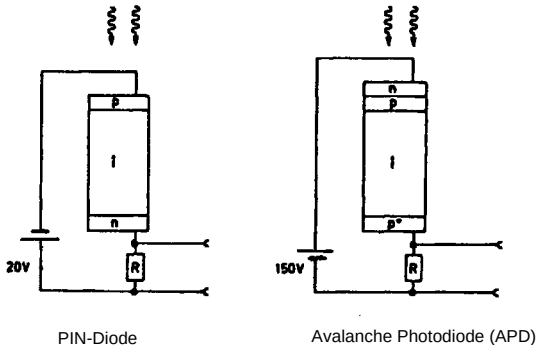

Figure 16 – Photodiodes for optical systems.

Figure 16 depicts an APD, this component has except for the pn-junction and the intrinsic zone a highly doped p+-zone. In this case we receive besides the constant electric field in the i-zone a very high field at the pn-junction (see also voltages for comparison).

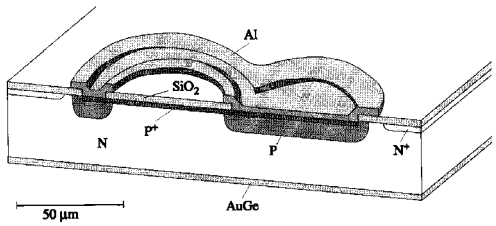

Figure 17 – Schematic structure of a Ge-APD [17].

This arrangement causes such a high acceleration of charge carriers that collisions occur between the electrons, produced by the absorption process, and the atoms of the semiconductor material. Thus, further electrons will be freed from the atoms (lifted from the valence band into the conduction band) and we receive secondary electrons. This effect is called “impact ionization”. The secondary electrons are now also accelerated and generate tertiary electrons and so on, which leads to an avalanche. As a result the APD possesses an internal gain and thus it is a very proper component for optical systems. The small geometrical size enables small junction capacities (see Fig. 17) and therefore, high cut-off frequencies are gained. Typical diameters of high bit rate photodiodes are in the order or 50 µm.

Most common materials for application in

photodiodes are silicon (Si), germanium (Ge) and gallium indium arsenide phosphide (GaInAsP). Figure 18 shows the proper use according to the relative sensitivity versus wavelength (see also Fig. 19).

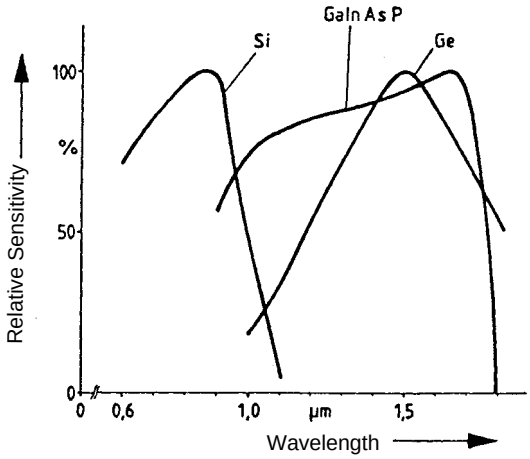

Figure 18 – Spectral sensitivity of photodiodes.

Fig.19 shows a summary of the most important components and their properties for fiber-optic transmission systems: In 1973 there was a fiber featuring a first minimum at a wavelength of about 850 nm in the order of 5 dB/km. Therefore, fiber-optic transmission started at the area of this wavelength and thus, this area is called the "first window". In 1981, the attenuation lowered to about 0.5 dB/km and 0.3 dB/km at 1300 nm and 1550 nm respectively. Hence, the areas at these wavelengths are called the "second" and the "third window" where fiber-optic communication systems operate: Today's fibers reach an absolute minimum of 0.176 dB/km due to principle physical effects as described above: Rayleigh scattering and infrared self-absorption.

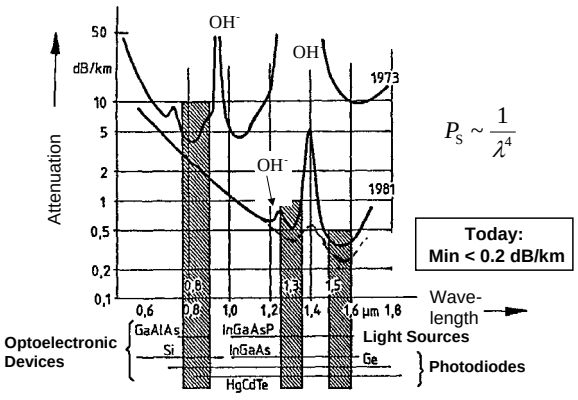

Figure 19 – Spectral attenuation of optical fibers and useful wavelengths of optoelectronic devices.

As optoelectronic components for light sources, we apply GaAlAs LEDs and laser diodes for the first window and InGaAsP devices, for the second and the third one. Photodiode materials are the well known Si for 850 nm, Ge and InGaAsP for the wavelength range of about 1200 nm to over 1600 nm. Furthermore, mercury cadmium telluride (HgCdTe) materials are very promising compounds for future optical detectors [35].

IV. FIBER-OPTIC TRANSMISSION SYSTEMS

Using the devices described above, fiber-optic transmission systems could be developed applying optoelectric and electrooptic components for transmitters and receivers as well as a fiber in the center of the arrangement (see Fig.1).

However, an optical communication system is more than a light source a fiber and a photodiode. There is a laser driver circuit necessary to provide a proper high bit rate electric signal; this driver combined with a laser or an LED build the optical transmitter. As well the photodiode (pin or APD) together with the front-end amplifier form the optical detector, also called "optical receiver" (see Fig.20).

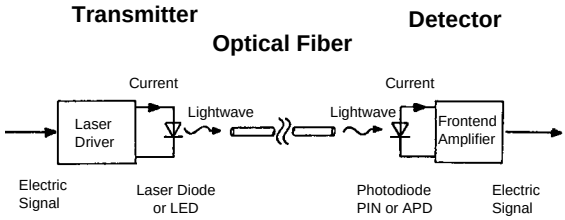

Figure 20 – Optical fiber transmission principle.

This front-end amplifier consists of a very highly sophisticated electric circuit. It has to detect a high bandwidth operating with very few photons due to a large fiber length and it is struggling with a variety of noise generators.

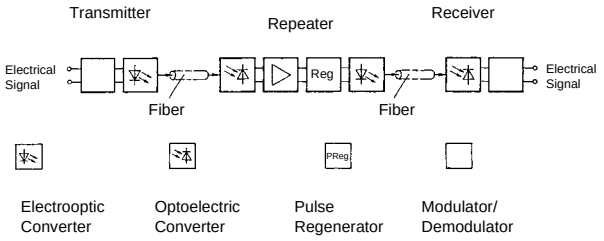

Figure 21 – Transmitter, repeater and receiver.

However, if the desired link length cannot be realized, a repeater will be inserted consisting of a front-end amplifier and a pulse regenerator (see Fig.21). This pulse regenerator is necessary to restore the data signal before it is fed to a further laser driver followed by another laser. Figure 22 visualizes the immense capability of the data regeneration: Directly at the front-end amplifier, (1) the eye pattern and the data signal cannot be detected as those. After a first following equalizer circuit, eye pattern and data signal are hardly recognized (2), whereas both are quite well restored after a second equalizer step (3). The non-return to zero signal at 168 Mbit/s can be seen clearly. Finally, a low pass filter is applied to suppress very high frequency noise (4).

At this point, it must be mentioned that an optical communication system is still more than discussed in this paper: There are further electric circuits to be taken into account, such as circuits for coding, scrambling, error correction, clock extraction, temperature power-level and gain controls [19].

Furthermore, until now, we have described a unidirectional system exclusively (see Fig. 23), i.e. we think of a telephone link at which a person at one side of

the link is able to speak. At the other side of the link a second person can listen exclusively, but the system does not operate the other way round. To overcome this insufficient situation, optical couplers on both sides of the link are inserted. Therefore, we achieve a bi-directional system [20]. The two counter propagating optical waves superimpose undisturbed, they separate at the optical couplers on the other side of the link and reach the according receivers. To improve the transmission capacity drastically, wavelength selective couplers are applied, called "multiplexers" and "demultiplexers". Several laser diodes operating at different wavelengths are used as transmitters; their light waves are combined by the multiplexer and on the other link end separated by the demultiplexer.

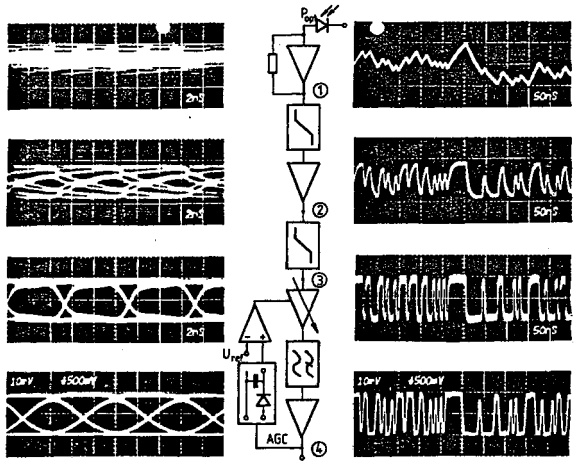

Figure 22 – Eye pattern and data signal [18].

The set-up is named "wavelength division multiplex system" (WDM). If we apply this arrangement again in the two counter propagating directions, we achieve a bi-directional WDM system [21]. The transmission capacity is risen by the number *N* of the channels transmitted over one single fiber.

Figure 24 depicts a scheme to describe the limits of optical transmission systems. For a single channel system two basic limitations occur. Such systems are called "direct detection systems", consisting of one laser one fiber and one detector.

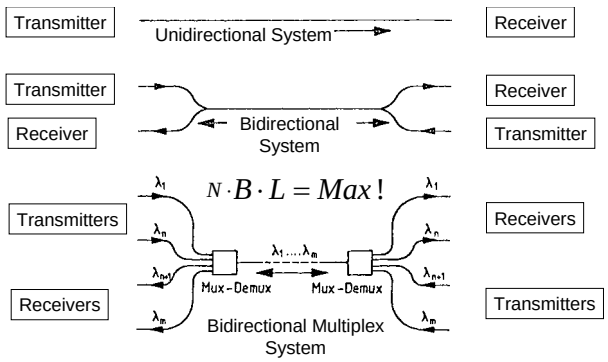

Figure 23 – Variety of optical transmission systems.

The limitations are divided into two groups, the systems suffer from attenuation limitation and dispersion limitation. The attenuation limited arm is governed by the transmitter power of the applied laser diode, the fiber attenuation and the receiver sensitivity of the detector. The dispersion limited arm is governed by the modulation bandwidth of the applied laser diode, the fiber dispersion and the demodulation bandwidth of the detector.

Thus, for high bit rate long distance transmission systems, exclusively high speed lasers and photodiodes will be installed as well as a monomode fiber. Figure 25 shows the eye pattern of a 43 Gbit/s data signal transmitted over a single channel high bit rate system. The data rate corresponds to the cut-off frequency of about 30 GHz which is approximately the highest frequency a single laser diode can be modulated.

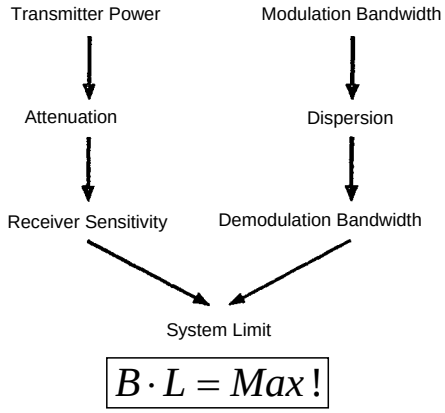

Figure 24 – Limits of optical transmission systems.

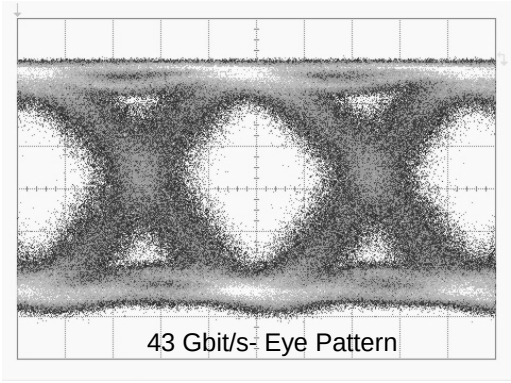

Figure 25 – Eye pattern of a high bit rate data signal [22].

V. CONCLUSIONS AND OUTLOOK

The aim of this paper was to give an introduction to fiber transmission systems, working with basic components. The reader should be familiarized with the fundamental optical techniques for communication systems. However, for more comprehensive considerations there are further components to be dealt with [23], e.g. the optical amplifier to enhance the link length over the conventional limits described above. In order to do that, Erbium and Raman amplifiers [24 -26] have been developed to overcome the problem of attenuation in fibers.

Moreover, it is also necessary to avoid signal distortions caused by the dispersion mechanisms in optical fibers. The solution to that problem could be the use of soliton transmission [27, 28]. The principle idea has been developed more than 20 years ago but it came

just recently as product on the optical telecom market. For very high data rates such as over 40 Gbit/s, polarization problems in fibers have to be considered. There is a further distortion called “polarization mode dispersion (PMD)” which leads again to pulse broadening and therefore to bandwidth reduction with impact on the transmission capacity, the product of bandwidth and fiber length [12, 29]. In this paper only point-to-point links have been discussed. Further applications for future optical systems must be taken into account - such as optical networks [30-32] (LAN and MAN).

Finally, the subject of opening up the last mile for fiber communication is of great interest. Yet, more than ten years this idea of fiber to the home (FTTH) is discussed but it is still too expensive and therefore still waiting to reach the commercial market. May be new plastic fibers [33] with sufficient low attenuation and gradient profile together with high-speed LEDs [34] could solve this problem in the near future.

REFERENCES

[1] Maiman, T. H.: Optical and Microwave-Optical Experiments in Ruby. Phys. Rev. Lett. 4 (1960)11, 564

[2] Quist, T. M. et al.: Semiconductor Maser of GaAs. Appl. Phys. Lett. 1 (1962) 4, 91

[3] Kapron, F. P. et al.: Radiation Losses in Glass Optical Waveguides. Appl. Phys. Lett. 17 (1970) 10, 423

[4] Adams, W G.; Day, R. E.: The Action of Light an Selenium. Proc. R.Soc. 25 (1876) 113

[5] Marstaller, A.: private communication

[6] Kao, C. K.; Hockham, G. A.: Dielectric-Fiber Surface Waveguides for Optical Frequencies. Proc. IEE 113 (1966) 7, 1151

[7] Börner, M.: German Patent 1254513: Mehrstufiges Übertragungssystem für in Pulscodemodulation dargestellte Nachrichten.

[8] Miller, S. E. et al.: Research Toward Optical-Fiber Transmission Systems. Proc. IEEE 61 (1973) 12, 1703

[9] Gloge, D. et al.: Multimode Theory of Graded Core Fibers. Bell Syst. Techn. J. 52 (1973) 1563

[10] Marcuse, D.: Calculation of Bandwidth from Index Profiles of Optical Fibers. 1: Theory. Appl. Opt. 18 (1979) 12, 2073

[11] Cohen, L. G. et al.: Dispersion and Bandwidth Spectra in Single-Mode Fibers. IEEE J. Quant. Electr. QE-18 (1982) 1, 49

[12] Mahlke, G.; Gössing, P: Fiber Optic Cables Siemens AG Berlin - Munich: Publicis-MCD-Verlag, Erlangen, 77

[13] Burrus, C. A.; Miller, B. I.: Small Area Double Heterostructure AlGaAs Electroluminescent Diode Sources for Optical-Fiber Transmission Lines. Opt. Commun. 4 (1971) 4, 307

[14] Panish, M. B.: Heterostructure Injection Lasers. Proc. IEEE 64 (1976) 10, 1512

[15] Melchior, H. et. al.: Photodetectors for Optical Communication Systems. Proc. IEEE 58 (1970) 10, 1466

[16] Pearsall, T P.: Photodetectors for Optical Communication. J. Opt. Commun. 2 (1981) 2, 42

[17] Ebbinghaus, G. et al.: Small Area Ion Implanted p+n Germanium Avalanche Photodiodes for a Wavelength of 1.3 gm. Siemens Research and Development Report 14 (1985) 6, 284

[18] Kaiser, N., SEL-Alcatel Stuttgart, private communication.

[19] Drullmann, R.; Kammerer, W.: Leitungscodierung und betriebliche Überwachung bei regenerativen Lichtleitkabelübertragungssystemen. Frequenz 34 (1980) 2, 45

[20] Köster, W: Einfluss des Rückstreulichts auf die Nebensprechdämpfung in bidirektionalen Übertragungssystemen. Frequenz 37 (1983) H.4, 87

[21] Fußgänger, K.; Roßberg, R.: Uni and bidirectional 4λ x560 Mbit/s Transmission Systems Using WDM Devices and Wavelength-Selective Fused Single-Mode Fiber Couplers. IEEE J. Select. Areas in Commun.8 (1990) 6, 1032

[22] Wedding, B., SEL-Alcatel Stuttgart, private communication.

[23] Strobel, O. A.: Limits and New Trends in Fiber-Optic Transmission, to be published.[24] Payne, D. N. et al.: Fiber Optical Amplifiers, Proc. OFC '90, Tutorial, paper ThFl, S. 335, San Francisco, 1990

[25] Flannery, D.: Raman amplifiers: powering up for ultra-long-haul. Fiber Systems 5 (2001) 7, 48

[26] McCarthy, D. C.: Growing by Design. Photonics Spectra, July 2001, 88

[27] Mollenhauer, L. F.; Stolen, R. H.: Solitons in Optical Fibers. Fiberoptic Technol. April (1982) 193

[28] Malyon, D. J. et. al.: Demonstration of Optical Pulse Propagation over 10 000 km of Fiber Using Recirculating Loop. Electr. Lett. 27 (1991) 2, 120

[29] Chbat, M. W.: Managing Polarization Mode Dispersion. Photonics Spectra, June 2000, 100

[30] Sykes, E.: Modelling Sheds Light an Next-Generation Networks. Fiber Systems 5 (2001) 3, S. 58

[31] Weiershausen, W et al.: Realization of Next Generation Dynamic WDM Networks by Advanced OADM Design. Proc. Europ. Conf. on Networks and Optical Comm. 2000 (NOC 2000) 199

[32] Pfeiffer, T et al.: Optical Packet Transmission System for Metropolitan and Access Networks with more than 400 Channels. J. Lightw. Techn. 18 (2001) 12, 1928

[33] Kenward, M.: Plastic Fiber Homes in/on Low-Cost Networks. Fiber Systems 5 (2001) 1, S. 35

[34] Fiber Systems 4 (2000) 5, 14

[35] Lee, T.P.: Prospects and Challenges of Optoelectronic Components in Optical Network Systems. Seminar on Internat. Exchange & Techn. Co-operation, Sept. 22 - 24, 2001, Wuhan, China

Prof. Dr.-Ing. Dr. h.c. Otto Strobel, born in 1950 completed an apprenticeship in electrical engineering at DaimlerChrysler Stuttgart, Germany (former Daimler-Benz AG) in 1968. He received a diploma degree in physics from the department of physics at the Technische

Universität Berlin, Germany in 1980. From 1981 to 1988, he worked as scientist and head of laboratories for research and development of wave guides at Alcatel-SEL in Stuttgart. In 1986, he received a Dr.-Ing. degree from the department of electrical engineering at the Technische Universität Berlin. In 1988, he was appointed as professor for physics and optoelectronics at the Esslingen University of Applied Sciences, Germany. In 2001, he was awarded by a Dr. honoris causa degree from the Technical University Moscow Aviation Institute, Russia, and in the same year he got an appointment as a member of the Construction Consultative Committee of Wuhan Optics Valley of China. At Esslingen University of Applied Sciences, he actually is responsible for education in physics and optoelectronics; furthermore, he is vice dean of the faculty of basic sciences and director of the physics laboratory. His fields of interest are in the area of experimental physics, optoelectronics, integrated optics, fiber-optic communication and fiber-optic sensors.
Email: otto.strobel@fht-esslingen.de

Utilização do Método FDFD para a Análise dos Modos TM, Propagantes em Estruturas Periódicas 2-D

Paulo A. dos S. Ramalho e Carlos L. da S.S. Sobrinho

Departamento de Engenharia Elétrica e de Computação (DEEC) - Universidade Federal do Pará (UFPA)
Laboratório de Análise Numérica em Eletromagnetismo (LANE) - Universidade Federal do Pará (UFPA)
Belém, PA, Brasil 66075-900

***Resumo* — Na formulação desenvolvida neste trabalho, parte-se das equações de Maxwell no domínio da freqüência, e então obtém-se a equação de onda que rege a propagação dos modos TM em estruturas periódicas bidimensionais com anisotropia biaxial. Esta equação é então solucionada numericamente através método das diferenças finitas no domínio da freqüência (método FDFD). Visto que tal solução resulta vantajosamente em um problema de autovalores convencional, onde a matriz característica é esparsa, torna-se bastante vantajosa, a solução computacional do problema. No entanto, para garantir a eliminação dos modos espúrios, problema que se verifica em muitas formulações, é imposta, nesta solução, a condição do divergente do vetor indução magnética igual a zero. O objetivo principal deste trabalho é estabelecer uma relação de dependência entre as características de propagação para estruturas periódicas bidimensionais, e as suas características geométricas.**

***Palavras Chave* – Estruturas Periódicas, método FDFD, modo TM.**

I. INTRODUÇÃO

Durante as últimas décadas, o estudo de estruturas periódicas sob o ponto de vista da propagação de ondas vem alcançando uma grande importância em diversas áreas do conhecimento, tais como, a acústica, a sismologia e a área das comunicações ópticas. Onde nesta última, tais estruturas são conhecidas como Cristais Fotônicos.

Os cristais fotônicos consistem de dielétricos organizados de forma periódica no espaço, visto que, devido a esta periodicidade, é possível o controle da propagação da luz ao longo de sua estrutura, haja vista que, em determinadas faixas de freqüências, chamadas de PBG (*Photonic Band Gap*) [1], não há propagação das ondas eletromagnéticas na estrutura do cristal.

Os cristais fotônicos podem ser empregados na fabricação de cavidades ópticas [2]-[3], e também em guias e filtros ópticos. Estes materiais, são aplicados também, como isolação entre as portas Tx e Rx em antenas de microfita [4], e são empregados ainda, como refletores parabólicos em antenas diretivas [5].

Na formulação apresentada neste trabalho, foi utilizado de forma eficiente o método FDFD [6,7] na análise da propagação dos modos TM em estruturas periódicas constituídas de materiais com anisotropia biaxial. A solução numérica através deste método, resulta em um problema convencional de autovalores, onde a matriz característica é esparsa e somente os valores não nulos precisam ser armazenados. Apesar da formulação ser bastante abrangente, somente exemplos, considerando-se materiais isotrópicos foram considerados, neste trabalho.

II. TEORIA

Será mostrado agora, de forma clara e objetiva, o equacionamento para a obtenção da equação matricial que define o problema de autovalores, sendo que estes últimos, representam as freqüências dos modos propagantes nas estruturas dos cristais bidimensionais, os quais se quer analisar. A fim de alcançar tal objetivo, parte-se das equações de Maxwell no domínio da freqüência, e aplica-se o método das diferenças finitas (FDFD) [6,7], com o intuito de aproximar as derivadas parciais das equações por diferenças centradas, desta maneira facilitando o manejo matemático desta formulação. Este procedimento pode ser efetuado para dois tipos possíveis de propagação, que são: os modos transversais de propagação (modos TE e TM) e os modos de propagação oblíqua ao eixo da estrutura (os modos híbridos), como já explanado em trabalhos anteriores [6-8], no entanto, este trabalho trata somente do modo transversal TM.

Vale frisar que, quando se obtêm as curvas de dispersão, torna-se possível determinar as características das bandas proibidas (caso existam, freqüência central e largura de banda) com relação a variação dos parâmetros eletromagnéticos da estrutura sob análise.

II.1. DESCRIÇÃO DO PROBLEMA

Considere uma estrutura, com uniformidade segundo a direção longitudinal, e periódica nas direções transversais a esta. Define-se a direção longitudinal como a direção do eixo Z (fig. 1(a)). Sendo a e b o comprimento dos vetores independentes da rede cristalina, os quais formam a rede primária e apontam nas direções x e y, respectivamente. Esta rede representa toda a estrutura periódica do cristal bidimensional. Sendo que a seção transversal deste cristal é mostrada na fig. 1(b).

Nota-se que, a área da figura dentro de uma célula se repete segundo as direções dos vetores de treliça. Essa figura nada mais é, do que o perfil de permissividade elétrica dentro da rede cristalina. Este perfil pode ser tanto isotrópico quanto anisotrópico, podendo ser, ainda, gradual ou em degraus segundo as direções dos vetores a

e b, contudo sendo uniforme segundo a direção z. Na formulação desenvolvida neste trabalho, os meios foram considerados não magnéticos ($\mu = \mu_o$) e com anisotropia biaxial.

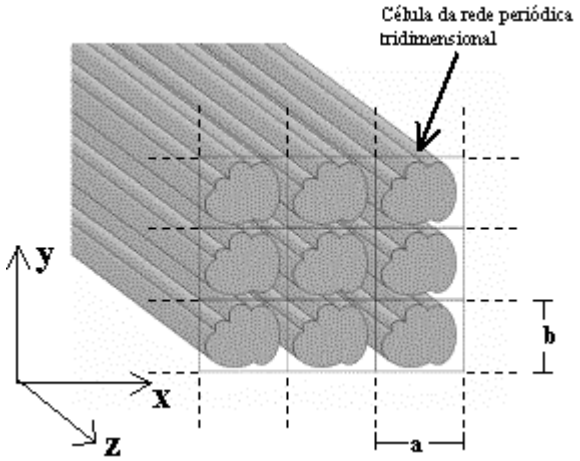

(a)

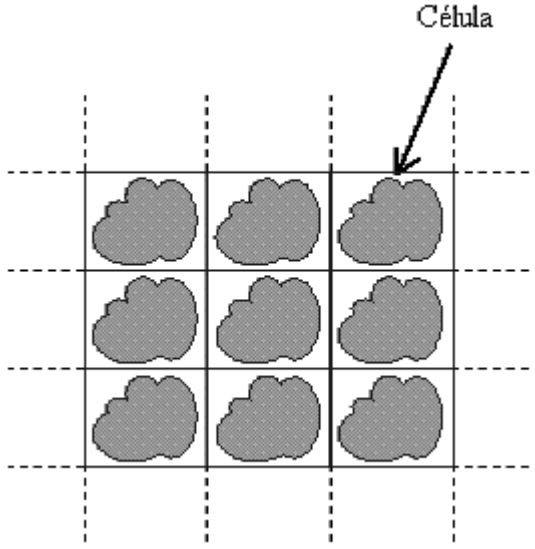

(b)

Figura 1. Estrutura periódica dielétrica bidimensional e anisotrópica. (a) Visualização tridimensional. (b) Seção transversal.

Depois de descrever as características do cristal, o passo seguinte é encontrar a equação de onda que rege a propagação em tais estruturas periódicas e, então, resolve-la numericamente mediante o uso do método FDFD. E é isso que é feito nas seções posteriores.

II.2. CARACTERIZAÇÃO DOS MODOS PROPAGANTES TM PARA O CRISTAL FOTÔNICO BIDIMENSIONAL

Para as estruturas estudadas neste trabalho, considera-se que o meio é não-magnético e os campos têm dependência harmônica no tempo da forma $exp(j\omega t)$, onde $\omega = 2\pi f$, definida como sendo a freqüência angular. Deste modo, deve-se representar as equações de Maxwell no domínio da freqüência [9] nas formas

$$\nabla \times \overline{E} = -j\omega\mu_o \overline{H} \tag{1}$$

$$\nabla \times \overline{H} = j\omega [\varepsilon] \overline{E} \tag{2}$$

$$\nabla \cdot \left([\varepsilon] \overline{E} \right) = 0 \tag{3}$$

$$\nabla \cdot \left(\mu_o \overline{H} \right) = 0 \tag{4}$$

onde $\overline{E}$ é o vetor intensidade de campo elétrico, $\overline{H}$ é o vetor intensidade de campo magnético e $[\varepsilon]$ é o tensor permissividade . Considerando que as estruturas analisadas, como outrora foi dito, possuem permissividade anisotrópica biaxial, logo para um sistema de eixos de coordenadas coincidentes com o sistema de eixos óticos do cristal, $[\varepsilon]$ deve ser definido como:

$$[\varepsilon] = \varepsilon_o \begin{bmatrix} \varepsilon_x(\bar{r}) & 0 & 0 \\ 0 & \varepsilon_y(\bar{r}) & 0 \\ 0 & 0 & \varepsilon_z(\bar{r}) \end{bmatrix}, \tag{5}$$

considerando que ε_o é a permissividade do espaço livre e que $\bar{r} = x\,\hat{i} + y\,\hat{j}$ é o vetor posição, logo, devido a periodicidade, tem-se que:

$$\varepsilon_i\left(\bar{r} + m\bar{p}_1 + n\bar{p}_2\right) = \varepsilon_i(\bar{r}); \qquad i = x, y, z, \tag{6}$$

onde m e n são inteiros arbitrários, $\bar{p}_1$ e $\bar{p}_2$ são os vetores primitivos da rede cristalina primária, com $\left\|\bar{p}_1\right\| = a$ e $\left\|\bar{p}_2\right\| = b$, e $\varepsilon_x, \varepsilon_y, \varepsilon_z$ são as permissividades relativas efetivas em relação aos eixos *x, y* e *z*, respectivamente.

O problema analisado neste trabalho, considera que ao longo da direção *z*, a propagação é da forma $e^{-\gamma_z z}$, onde γ_z é a constante de propagação, então as equações (1)-(4) ficam na forma matricial

$$\begin{bmatrix} H_x \\ H_y \\ H_z \end{bmatrix} = \frac{j}{\omega\mu_o} \begin{bmatrix} \dfrac{\partial E_z}{\partial y} + \gamma_z E_y \\ -\gamma_z E_x - \dfrac{\partial E_z}{\partial x} \\ \dfrac{\partial E_y}{\partial x} - \dfrac{\partial E_x}{\partial y} \end{bmatrix}, \tag{7}$$

$$\begin{bmatrix} E_x \\ E_y \\ E_z \end{bmatrix} = \frac{1}{j\omega\varepsilon_o} \begin{bmatrix} \varepsilon_x^{-1}(\bar{r})\left(\dfrac{\partial H_z}{\partial y} + \gamma_z H_y \right) \\ \varepsilon_y^{-1}(\bar{r})\left(-\gamma_z H_x - \dfrac{\partial H_z}{\partial x} \right) \\ \varepsilon_z^{-1}(\bar{r})\left(\dfrac{\partial H_y}{\partial x} - \dfrac{\partial H_x}{\partial y} \right) \end{bmatrix}, \tag{8}$$

$$\frac{\partial \varepsilon_x(\bar{r}) E_x}{\partial x} - \frac{\partial \varepsilon_y(\bar{r}) E_y}{\partial y} - \gamma_z \varepsilon_z(\bar{r}) E_z = 0, \tag{9}$$

$$\mu_o \left(\frac{\partial H_x}{\partial x} - \frac{\partial H_y}{\partial y} - \gamma_z H_z \right) = 0. \tag{10}$$

É freqüente, considerarem-se os casos de propagação oblíqua e transversal, na análise dos modos propagantes, porém, como já citado anteriormente, será considerado no trabalho apenas o caso de propagação transversal TM, na análise dos modos propagantes. A propagação transversal, é onde se analisa os modos que possuem $\gamma_z = 0$ e que podem ser separados em modos TE e TM (fig. 2(a)), a qual já é diferente da propagação oblíqua, que é aquela onde deseja-se determinar as características de dispersão dos modos que possuem $\gamma_z \neq 0$ e que têm a característica de serem modos híbridos (fig. 2(b)).

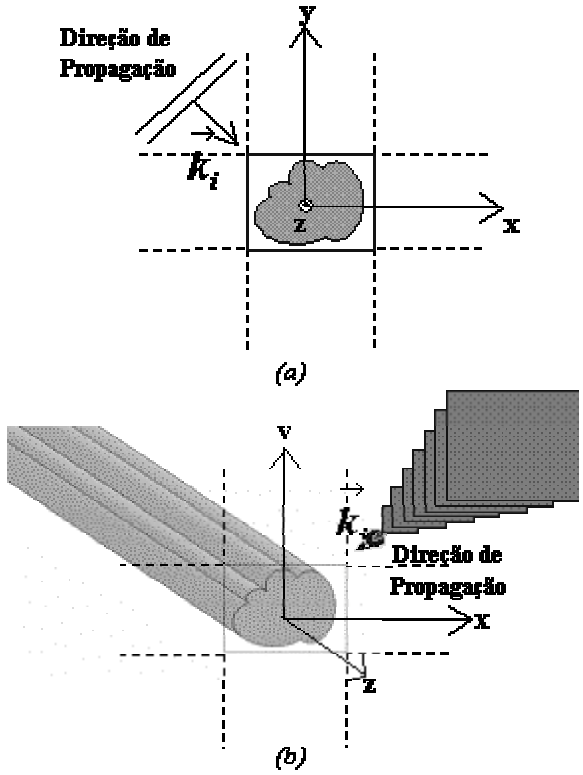

Figura 2. Esquemas de propagação para uma célula. (a) Transversal. (b) Oblíqua.

Na propagação transversal, a componente E_z é utilizada para a obtenção dos modos TM e a componente H_z é utilizada para a obtenção dos modos TE. No caso da propagação oblíqua, a formulação pode ser desenvolvida através das componentes transversais H_x e H_y do campo magnético, pois neste caso, quando é realizada a inclusão da condição de divergente do campo magnético (ou através das correspondentes do campo elétrico) igual a zero ($\nabla \cdot (\mu_o \overline{H}) = 0$), contorna-se o problema dos modos espúrios.

Propagação Transversal TM.

No caso da propagação transversal, quando $\gamma_z = 0$, os modos podem ser separados em TE e TM., A formulação para este caso torna-se mais simples, pois é feita usando apenas uma componente de campo.

Considerando o modo TM, tem-se que $\gamma_z = 0$ e $H_z = 0$. Desta forma, das equações (7) e (8) obtêm-se:

$$E_x = 0, \tag{11}$$

$$E_y = 0, \tag{12}$$

$$E_z = \frac{1}{j\omega\varepsilon_0\varepsilon_z}\left(\frac{\partial H_y}{\partial x} - \frac{\partial H_x}{\partial y}\right), \tag{13}$$

$$H_x = \frac{j}{\omega\mu_0}\frac{\partial E_z}{\partial y}, \tag{14}$$

$$H_y = -\frac{j}{\omega\mu_0}\frac{\partial E_z}{\partial x}, \tag{15}$$

Substituindo (14) e (15) em (13), resulta em

$$j\omega\varepsilon_0\varepsilon_z E_z = \frac{\partial}{\partial x}\left(\frac{-j}{\omega\mu_0}\frac{\partial E_z}{\partial x}\right) - \frac{\partial}{\partial y}\left(\frac{j}{\omega\mu_0}\frac{\partial E_z}{\partial y}\right),$$

ou

$$k_0^2\varepsilon_z E_z + \frac{\partial^2 E_z}{\partial x^2} + \frac{\partial^2 E_z}{\partial y^2} = 0, \tag{16}$$

onde, $k_0 = \omega\sqrt{\mu_0\varepsilon_0}$, é o numero de onda do espaço livre. Em (16), tem-se a equação de onda que define a propagação dos modos TM, para E_z. Deve-se notar que como $\gamma_z = 0$, a condição $\nabla \cdot \mathbf{H} = 0$ é garantida. Para provar isso basta observar de (14) e (15) que $\frac{\partial H_x}{\partial x} = -\frac{\partial H_y}{\partial y}$. Desta maneira, os modos espúrios são evitados.

Na formulação de problemas que envolvem periodicidade, de forma geral usa-se como ponto inicial, o teorema de Floquet [10,11]. Sendo que o mesmo, quando aplicado ao problema em análise, implica na condição de contorno,

$$V(x+a, y+b) = e^{-j\beta_x a - j\beta_y b} V(x,y), \tag{17}$$

onde $V(x,y) = V(\bar{r})$ é qualquer componente de campo e, β_x e β_x são as constantes de fase nas direções dos eixos *x* e *y*, respectivamente. Portanto, a fim de que este problema possa ser resolvido a partir de uma única célula da estrutura, a expressão (17) deve ser aplicada, então, para a componente E_z, tem-se:

$$E_z\Big|_{x=a} = E_z\Big|_{x=0} e^{-j\beta_x a}, \tag{18}$$

$$E_z\Big|_{y=b} = E_z\Big|_{y=0} e^{-j\beta_x b}, \tag{19}$$

Tal condição garante que, todo vetor de onda fora da zona irredutível de Brillouin será refletido automaticamente, através de translação, para um vetor equivalente dentro da mesma.

A – A aplicação do método FDFD na solução numérica da equação (16)

Agora será empregado o método das diferenças finitas no domínio da freqüência na solução da equação (16). Neste caso, considera-se a seção transversal de uma única célula da estrutura periódica com visto na fig. 3(a). No entanto, a solução aproximada considera a mesma célula definida através de uma malha gradual de pontos, como mostrado na fig. 3(b). Após o que, pode-se destacar um único ponto desta malha, o que é feito através da célula gradual dos cinco pontos (fig. 4), que é tomada como base para a obtenção da solução numérica da equação (16).

Expandindo a componente E_z em série de Taylor, ao redor do ponto P, obtêm-se as derivadas de segunda ordem, sendo que o ponto P tem como vizinhos, os pontos N, S, E e W, apresentados na fig. 4. Assim, as derivadas de segunda ordem são obtidas de forma aproximada, o que é feito pelo truncamento das séries até os termos com o quadrado da distância, e também pela substituição da componente E_z por E, como segue:

$$E_{N_{1,4}} \cong E_P + n\left.\frac{\partial E}{\partial y}\right|_{1,4} + \frac{1}{2}n^2\left.\frac{\partial^2 E}{\partial y^2}\right|_{1,4}, \qquad (20)$$

$$E_{S_{2,3}} \cong E_P - s\left.\frac{\partial E}{\partial y}\right|_{2,3} + \frac{1}{2}s^2\left.\frac{\partial^2 E}{\partial y^2}\right|_{2,3}, \qquad (21)$$

$$E_{E_{3,4}} \cong E_P + e\left.\frac{\partial E}{\partial x}\right|_{3,4} + \frac{1}{2}e^2\left.\frac{\partial^2 E}{\partial x^2}\right|_{3,4}, \qquad (22)$$

$$E_{W_{1,2}} \cong E_P - w\left.\frac{\partial E}{\partial x}\right|_{1,2} + \frac{1}{2}w^2\left.\frac{\partial^2 E}{\partial x^2}\right|_{1,2}, \qquad (23)$$

Nas equações de (20) a (23), os índices 1,2,3 e 4 são referentes aos respectivos meios da célula da fig. 4. Portanto, destas expressões é que se obtêm a forma aproximada das derivadas de segunda ordem, como é feito abaixo:

$$\left.\frac{\partial^2 E}{\partial y^2}\right|_{1,4} = \frac{2}{n^2}\left(E_{N_{1,4}} - E_P - n\left.\frac{\partial E}{\partial y}\right|_{1,4}\right), \qquad (24)$$

$$\left.\frac{\partial^2 E}{\partial y^2}\right|_{2,3} = \frac{2}{s^2}\left(E_{S_{2,3}} - E_P + s\left.\frac{\partial E}{\partial y}\right|_{2,3}\right), \qquad (25)$$

$$\left.\frac{\partial^2 E}{\partial x^2}\right|_{3,4} = \frac{2}{e^2}\left(E_{E_{3,4}} - E_P - e\left.\frac{\partial E}{\partial x}\right|_{3,4}\right), \qquad (26)$$

$$\left.\frac{\partial^2 E}{\partial x^2}\right|_{1,2} = \frac{2}{w^2}\left(E_{W_{1,2}} - E_P + w\left.\frac{\partial E}{\partial x}\right|_{1,2}\right), \qquad (27)$$

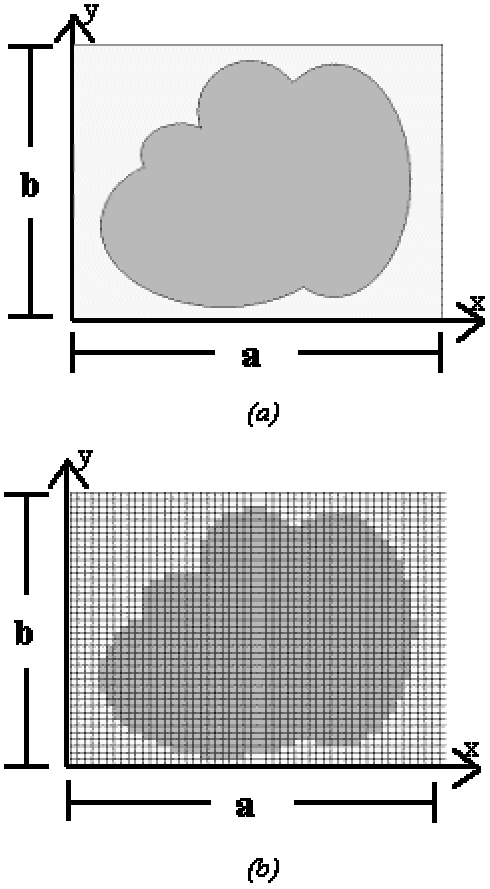

Figura 3. (a) Célula da rede sob análise. (b) A célula discretizada.

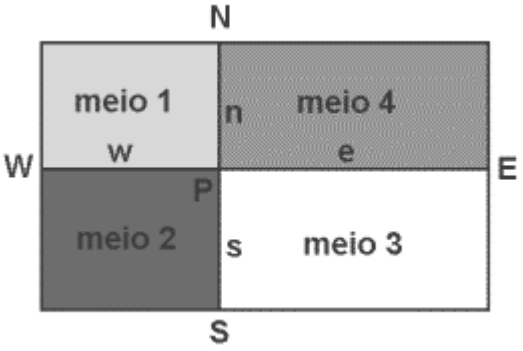

Figura 4. Célula gradual dos cinco pontos

Aplicando (16) para as quatro regiões da célula gradual dos cinco pontos (fig. 4), têm-se:

$$0 = k_0^2\varepsilon_{zi}E_P + \left.\frac{\partial^2 E}{\partial x^2}\right|_i + \left.\frac{\partial^2 E}{\partial y^2}\right|_i, \qquad (28)$$

onde o subscrito *i*, indica um dos quatro meios 1,2,3 ou 4.

Substituindo, nesta equação, as derivadas de 2ª ordem obtidas em (24) a (27), resulta:

Para a região 1

Nesta região, a fim de se ter uma maior praticidade matemática, multiplica-se a equação (28) por $wn/2$, e desta maneira encontra-se:

$$0 = wn\frac{k_0^2}{2}\varepsilon_{z1}E_p + \frac{n}{w}\left[E_W - E_P + w\left.\frac{\partial E}{\partial x}\right|_1\right] + \frac{w}{n}\left[E_N - E_P - n\left.\frac{\partial E}{\partial y}\right|_1\right], \quad (29)$$

Para a região 2

Pelo mesmo motivo explicado anteriormente, multiplica-se, agora (28) por $ws/2$.

$$0 = ws\frac{k_0^2}{2}\varepsilon_{z2}E_P + \frac{s}{w}\left[E_W - E_P + w\left.\frac{\partial E}{\partial x}\right|_2\right] + \frac{w}{s}\left[E_S - E_P + s\left.\frac{\partial E}{\partial y}\right|_2\right], \quad (30)$$

Para a região 3

Neste caso, multiplica-se (28) por $se/2$ e têm-se:

$$0 = es\frac{k_0^2}{2}\varepsilon_{z3}E_p + \frac{s}{e}\left[E_E - E_P + e\left.\frac{\partial E}{\partial x}\right|_3\right] + \frac{e}{s}\left[E_S - E_P + s\left.\frac{\partial E}{\partial y}\right|_3\right], \quad (31)$$

Para a região 4

Multiplica-se (28) por $ne/2$, resultando em:

$$0 = en\frac{k_0^2}{2}\varepsilon_{z4}E_p + \frac{n}{e}\left[E_E - E_P - e\left.\frac{\partial E}{\partial x}\right|_4\right] + \frac{e}{n}\left[E_N - E_P - n\left.\frac{\partial E}{\partial y}\right|_4\right], \quad (32)$$

Quando se somam as equações (29)-(32), resulta:

$$0 = \left\{\frac{k_0^2}{2}\left[wn\varepsilon_{z1} + ws\varepsilon_{z2} + es\varepsilon_{z3} + en\varepsilon_{z4}\right] - \left[\frac{n}{w} + \frac{w}{n} + \frac{s}{w} + \frac{w}{s} + \frac{s}{e} + \frac{e}{s} + \frac{n}{e} + \frac{e}{n}\right]\right\}E_P + \left[\frac{n+s}{e}\right]E_E + \left[\frac{n+s}{w}\right]E_W + \left[\frac{w+e}{n}\right]E_N + \left[\frac{w+e}{s}\right]E_S + Q \quad (33)$$

onde:

$$Q = n\left(\left.\frac{\partial E}{\partial x}\right|_1 - \left.\frac{\partial E}{\partial x}\right|_4\right) + s\left(\left.\frac{\partial E}{\partial x}\right|_2 - \left.\frac{\partial E}{\partial x}\right|_3\right) + w\left(\left.\frac{\partial E}{\partial y}\right|_2 - \left.\frac{\partial E}{\partial y}\right|_1\right) + e\left(\left.\frac{\partial E}{\partial y}\right|_3 - \left.\frac{\partial E}{\partial y}\right|_4\right) \quad (34)$$

B – Condições de Contorno.

Para que a continuidade das componentes H_x e H_y, do campo magnético seja garantida nas interfaces entre as quatro regiões da célula da fig. 4, as seguintes igualdades são obtidas de (14) e (15):

$$H_{x2} = H_{x1} \rightarrow \left.\frac{\partial E}{\partial y}\right|_2 = \left.\frac{\partial E}{\partial y}\right|_1, \quad (35)$$

$$H_{x3} = H_{x4} \rightarrow \left.\frac{\partial E}{\partial y}\right|_3 = \left.\frac{\partial E}{\partial y}\right|_4, \quad (36)$$

$$H_{y1} = H_{y4} \rightarrow \left.\frac{\partial E}{\partial x}\right|_1 = \left.\frac{\partial E}{\partial x}\right|_4, \quad (37)$$

$$H_{y2} = H_{y3} \rightarrow \left.\frac{\partial E}{\partial x}\right|_2 = \left.\frac{\partial E}{\partial x}\right|_3, \quad (38)$$

Com as condições impostas pelas equações (35) a (38), pode-se ver perfeitamente que em (34), $Q = 0$. Desta forma, (33) pode ser expressa como:

$$0 = \left\{\frac{k_0^2}{2}\left[wn\varepsilon_{z1} + ws\varepsilon_{z2} + es\varepsilon_{z3} + en\varepsilon_{z4}\right] - \left[\frac{n}{w} + \frac{w}{n} + \frac{s}{w} + \frac{w}{s} + \frac{s}{e} + \frac{e}{s} + \frac{n}{e} + \frac{e}{n}\right]\right\}E_P + \left[\frac{n+s}{e}\right]E_E + \left[\frac{n+s}{w}\right]E_W + \left[\frac{w+e}{n}\right]E_N + \left[\frac{w+e}{s}\right]E_S \quad (40)$$

Todavia, para uma continuidade desta formulação, com mais clareza, é melhor expressar (40), como:

$$-k_0^2 E_P = A_P E_P + A_E E_E + A_W E_W + A_N E_N + A_S E_S \quad , \tag{41}$$

onde:

$$A_P = -A_0\left(\frac{n}{w}+\frac{w}{n}+\frac{s}{w}+\frac{w}{s}+\frac{s}{e}+\frac{e}{s}+\frac{n}{e}+\frac{e}{n}\right) \quad , \tag{42}$$

$$A_0 = \frac{2}{wn\varepsilon_{z1} + ws\varepsilon_{z2} + es\varepsilon_{z3} + en\varepsilon_{z4}} \quad , \tag{43}$$

$$A_E = A_0\left(\frac{n+s}{e}\right) \quad , \tag{44}$$

$$A_W = A_0\left(\frac{n+s}{w}\right) \quad , \tag{45}$$

$$A_N = A_0\left(\frac{w+e}{n}\right) \quad , \tag{46}$$

$$A_S = A_0\left(\frac{w+e}{s}\right) \quad , \tag{47}$$

A equação (41) é a solução da equação (16) para um ponto P qualquer, da malha gradual da fig. 3(b). Ao aplicar tal equação, para todos os pontos da malha gradual, tem-se a solução geral para o problema, porém ao mesmo tempo que se faz isso, leva-se em conta, nesta generalização, as condições de contorno periódicas definidas em (18) e (19) para os pontos periféricos da malha.

Desenvolvendo a formulação para todos os pontos de uma malha gradual de $M \times N$ pontos, obtêm-se $(M-1)\times(N-1)$ equações, que podem ser representadas matricialmente na seguinte forma convencional de um problema de autovalores:

$$\left[(\mathrm{A}) - \lambda^2(\mathrm{I})\right](E) = 0 \tag{48}$$

onde (**I**) é a matriz identidade; $\lambda^2 = -k_0 = -(\omega/c)^2$ representa os autovalores, sendo *c* a velocidade da luz no espaço livre;

$$(E) = \left(E_{1,1}, E_{1,2}, E_{1,3}, \ldots, E_{1,N-1}, E_{2,1}, E_{2,2}, \ldots, E_{2,N-1}, \ldots, E_{M-1,N-1}\right)^T$$

contêm os autovetores; e (**A**), é uma matriz quadrada de ordem $(M-1)\times(N-1)$, na qual os elementos dependem dos parâmetros eletromagnéticos dos meios que constituem a estrutura e da sua geometria.

III. RESULTADOS OBTIDOS

Nesta etapa, são mostrados os resultados obtidos na análise de várias configurações de estruturas periódicas, onde o caso isotrópico foi considerado. Foram utilizadas estruturas com geometrias uniformes ao longo da direção *z*, apresentando periodicidade nas direções transversais (*x* e *y*). Neste trabalho foram realizadas análises de vários tipos de estruturas através do programa FotoTM_esp.exe, o qual foi desenvolvido em linguagem Fortran [12]. O código foi, então, adaptado para analisar as estruturas consideradas neste trabalho.

Foram analisados 9 tipos de estruturas periódicas, sendo que as células de cada estrutura são mostradas na fig. 5. Considerando que através do programa obtêm-se uma boa convergência a partir de uma malha de 400 pontos para a estrutura mostrada na fig. 5(a), como já verificado em [8]. Neste trabalho, a convergência foi obtida para uma malha de 33 × 33 pontos, para as estruturas mais complexas, pois existem geometrias consideradas que possuem círculos. Tais configurações necessitam de uma definição mais específica para os seus contornos, então esta malha passou a ser usada para todas as estruturas aqui consideradas. O programa foi executado, para todos as configurações mostradas na fig. 5, em um PC Pentium III 700 MHz com 128 MB de RAM, onde o sistema operacional *Windows 2000 professional* foi usado. Para a obtenção das características de propagação de cada estrutura, levou-se, aproximadamente, um tempo de cinco horas de processamento serial.

III.1. A ZONA DE BRILLOUIN

No que tange o estudo das características de propagação em cristais fotônicos, é de suma importância definir a chamada primeira zona de Brillouin [13-15]. Onde a mesma, é definida como sendo a célula primitiva de Wigner Seitz na rede cristalina recíproca tendo como localização, a origem do espaço de Fourier. A zona em questão possui valiosa importância, pois ela define a região no espaço dos vetores de onda que dão origem aos modos possíveis de propagação. Vetores de onda fora desta zona são refletidos automaticamente para um vetor equivalente dentro dela. Isso acontece devido as condições de contorno periódicas, as quais são usadas no tratamento de problemas de propagação em cristais fotônicos ou outros problemas que envolvam periodicidade.

Será visto nos resultados a seguir, que quando se analisam as características de dispersão dos modos propagantes TM nos cristais fotônicos com o valor do número de onda percorrendo o contorno da zona irredutível de Brillouin (fig. 6), obtém-se a largura efetiva da banda proibida de propagação.

III.2. APRESENTAÇÃO DOS RESULTADOS

A seguir são apresentados os resultados obtidos para as características de propagação de cada estrutura mostrada na fig. 5 (figuras 8-16 respectivamente), considerando-se a zona irredutível de Brillouin mostrada na fig. 6. O programa foi desenvolvido de forma que os

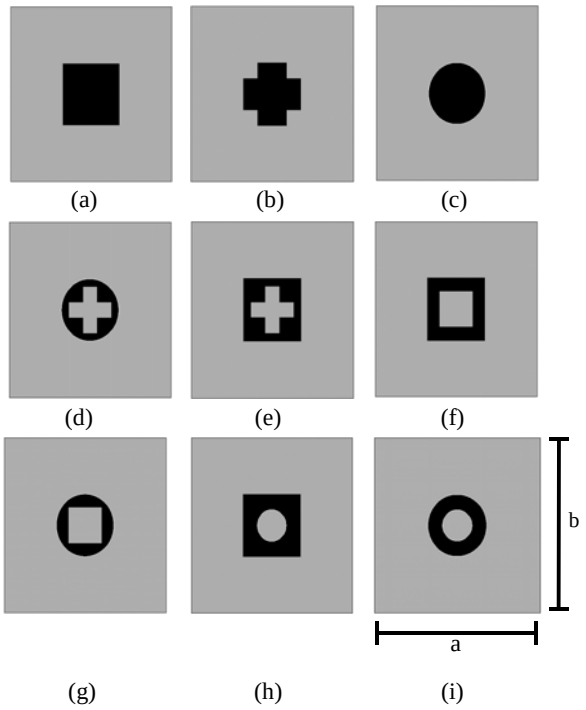

Figura 5 – Células das estruturas periódicas que foram analisadas. (a) Quadrado centrado; (b) Cruz centrada; (c) Círculo centrado; (d) Círculo centrado com orifício em forma de cruz; (e) Quadrado centrado com orifício em forma de cruz; (f) Quadrado centrado com orifício em forma de quadrado. (g) Círculo centrado com orifício em forma de quadrado. (h) Quadrado centrado com orifício circular (i) Anel centrado (rosca).

dados de saída são utilizados para caracterizar a geometria da célula de cada estrutura em análise, assim como para a obtenção das curvas de dispersão das mesmas. Vale ressaltar que os gráficos aqui mostrados foram obtidos através do *software* MATLAB 5.3 [16].

O valor de permissividade elétrica relativa da região mais escura das células é igual a ($\varepsilon_r = 8{,}9$), e no restante das mesmas igual a do espaço livre. Considera-se, assim como na formulação desenvolvida na seção anterior, os materiais utilizados como sendo não magnéticos ($\mu = \mu_o$). Vale ressaltar ainda que nas curvas de dispersão, para cada caso, têm-se no eixo vertical, a freqüência normalizada $\omega a / 2\pi c = a/\lambda$ e no eixo horizontal o valor do número de onda percorrendo o contorno da zona irredutível de Brillouin (Figuras 8-16).

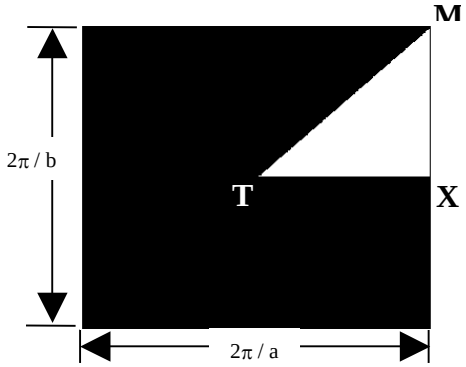

Figura 6 - Zona Irredutível de Brillouin (Região T-X-M-T).

Tabela I – Configurações geométricas da célula de cada estrutura

Estrutura	Figura	Dimensões
Quadrado centrado	5(a)	Lado = 0,3545a
Cruz centrada	5(b)	$d_A = d_B$ = 0,0886a e L=0,3545a
Círculo centrado	5(c)	Diâmetro = 0,3545a
Círculo centrado com orifício em forma de cruz	5(d)	Círculo externo: Diâmetro = 0,3545a
		Cruz interna: $d_A = d_B$ = 0,0443a e L=0,2658a
Quadrado centrado com orifício em forma de cruz	5(e)	Quadrado externo: Lado = 0,3545a
		Cruz interna: $d_A = d_B$ = 0,0443a e L=0,2658a
Quadrado centrado com orifício em forma de quadrado	5(f)	Quadrado externo: Lado = 0,3545a
		Quadrado interno: Lado = 0,2068a
Círculo centrado com orifício em forma de quadrado	5(g)	Círculo externo: Diâmetro = 0,3545a
		Quadrado interno: Lado = 0,2068a
Quadrado centrado com orifício circular	5(h)	Quadrado externo: Lado = 0,3545a
		Círculo interno: Diâmetro = 0,1772a.
Anel centrado (rosca).	5(i)	Círculo externo: Diâmetro = 0,3545a
		Círculo interno: Diâmetro = 0,1772a.

Tabela II – Características das Curvas de dispersão para cada estrutura

Estrutura	Faixa dos *Gaps*	Largura de Banda	Figura
Quadrado centrado	1º PBG - 0,3253 a 0,4417	0,1164	8
	2º PBG - 0,7787 a 0,7832	0,0045	
	3º PBG - 0,9266 a 0,9712	0,0446	
Cruz centrada	PBG - 0,3511 a 0,4660	0,0446	9
Círculo centrado	PBG - 0,3461 a 0,4643	0,1181	10
Círculo centrado com orifício em forma de cruz	1º PBG - 0,4306 a 0,4737	0,0431	11
	2º PBG - 0,8799 a 0,8904	0,0104	
Quadrado centrado com orifício em forma de cruz	1º PBG - 0,3889 a 0,4507	0,0618	12
	2º PBG - 0,8318 a 0,8646	0,0328	
	3º PBG - 0,9734 a 1,000	0,0265	
Quadrado centrado com orifício em forma de quadrado	1º PBG - 0,3966 a 0,4511	0,0546	13
	2º PBG - 0,8370 a 0,8716	0,0346	
	3º PBG - 0,9825 a 1,0291	0,0465	
Círculo centrado com orifício em forma de quadrado	1º PBG - 0,4413 a 0,4740	0,0327	14
	2º PBG - 0,8891 a 0,8946	0,0055	
Quadrado centrado com orifício circular	1º PBG - 0,3635 a 0,4450	0,0815	15
	2º PBG - 0,8010 a 0,8419	0,0409	
	3º PBG - 0,9460 a 0,9907	0,0447	
Anel centrado (rosca).	1º PBG - 0,3958 e 0,4678	0,0721	16
	2º PBG - 0,8439 e 0,8465	0,0026	

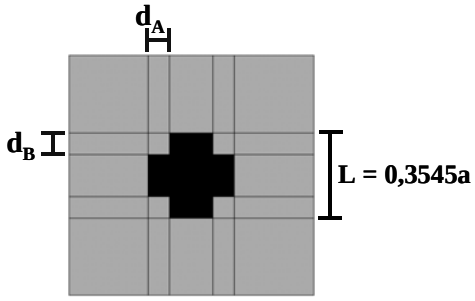

Figura 7. Parâmetros Geométricos da configuração cruz

Na tabela I são informadas as dimensões de cada estrutura analisada, bem como as figuras onde as mesmas são mostradas, onde a configuração de cruz obedece aos parâmetros expressos na figura 7.

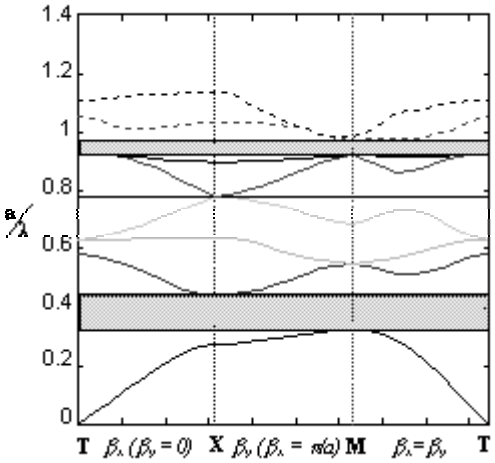

Figura 8. Características de propagação para a estrutura da Fig. 5(a)

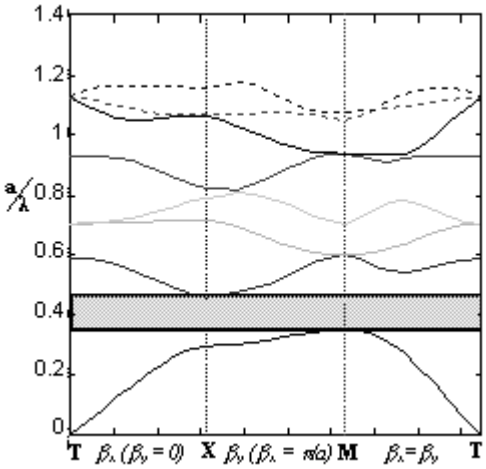

Figura 9. Características de propagação para a estrutura da Fig. 5(b).

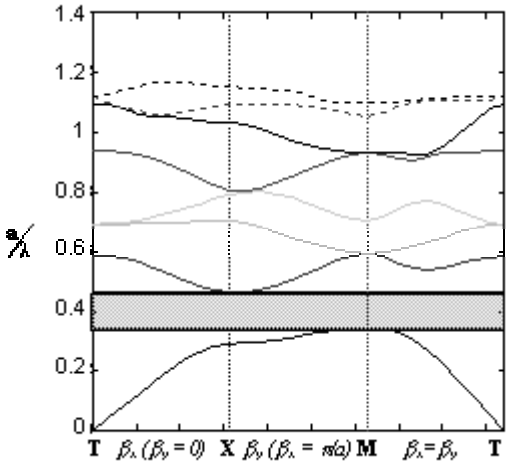

Figura 10. Características de propagação para a estrutura da Fig. 5(c).

Na tabela II, têm-se a informação sobre a faixa e a largura de banda (LB) dos *gaps* obtidos das respectivas curvas de dispersão de cada estrutura, sendo que a mesma tabela informa quais os números da figuras em que são mostradas as curvas.

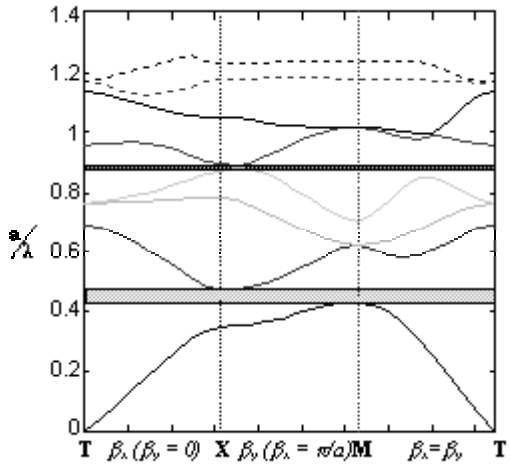

Figura 11. Características de propagação para a estrutura da Fig. 5(d).

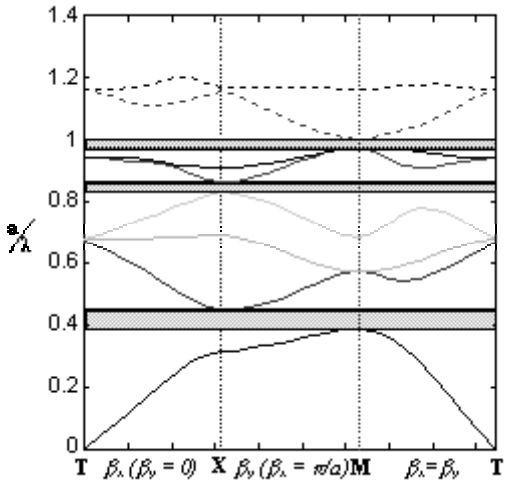

Figura 12. Características de propagação para a estrutura da Fig. 5(e).

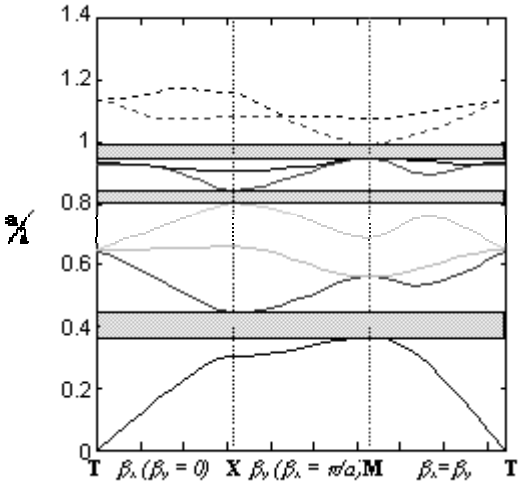

Figura 13. Características de propagação para a estrutura da Fig. 5(f).

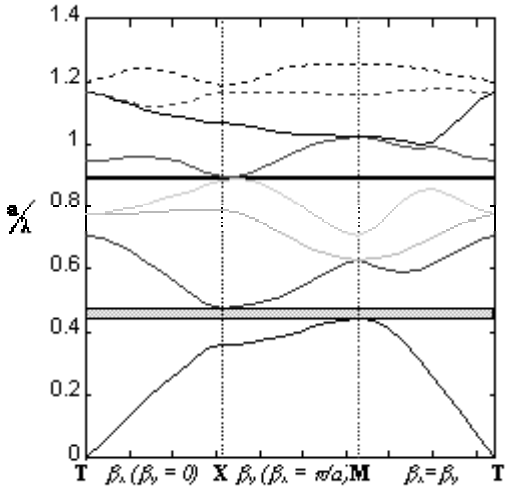

Figura 14. Características de propagação para a estrutura da Fig. 5(g).

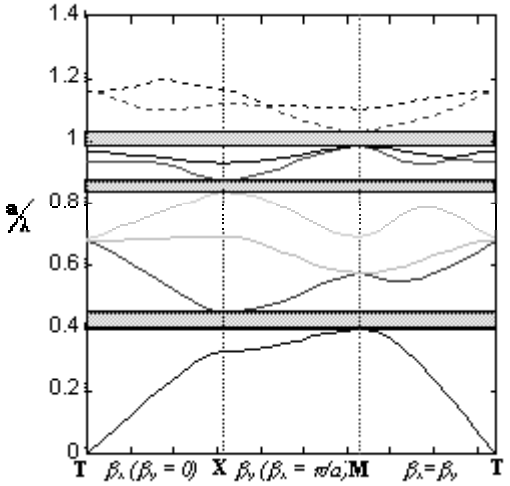

Figura 15. Características de propagação para a estrutura da Fig. 5(h).

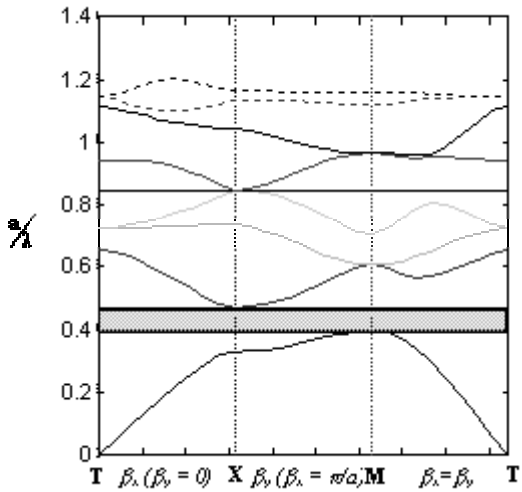

Figura 16. Características de propagação para a estrutura da Fig. 5(i).

III. CONCLUSÕES

O método das diferenças finitas no domínio da freqüência, demonstrou ser adequado para se analisar e projetar, os parâmetros de propagação de estruturas periódicas. Pois o mesmo foi empregado, com eficiência na solução numérica da equação de onda, que rege a propagação dos modos TM em estruturas periódicas bidimensionais, resultando vantajosamente em um problema de autovalores convencional, onde a matriz característica é esparsa e somente os valores diferentes de zero, da mesma, precisam ser armazenados.

As estruturas consideradas na formulação, foram investigadas de maneira que fossem encontrados *gaps* em freqüências nas suas características de propagação. Sendo que existem muitos dispositivos que utilizam as vantagens destes *gaps*, tais como: guias fotônicos; antenas de alta eficiência em freqüências de ondas milimétricas e de microondas; filtros seletivos em freqüência (FSS); blindagem óptica; cavidades ressonantes; acopladores direcionais; etc.

O objetivo da análise aqui apresentada foi o de investigar o que acontece com as características de dispersão de estruturas periódicas bidimensionais, quando as suas formas geométricas mudam. O que foi realizado para os modos transversais TM. Assim, observam-se quais delas apresentam resultados mais satisfatórios para uma dada aplicação. No entanto, a definição de melhor ou pior resultado, depende do objetivo de projeto que se quer alcançar.

No que diz respeito à largura de banda (LB), tem-se que dentre todas as características de propagação analisadas, o círculo apresentou um PBG com maior LB do que todos os outros casos analisados. Todavia, não fica atrás, o caso da cruz centrada, onde se obteve uma LB bem pronunciada no seu único *gap*, com um valor muito próximo da LB do *gap* único do círculo centrado

Vale ressaltar que em geral, o que se procura em um projeto é uma boa largura de banda do *gap*, pois dessa forma, surgem mais opções na hora de se escolher a freqüência de operação (ou comprimento de onda). Entretanto, quando se têm 3 PBGs com larguras de banda efetivas, em uma banda de análise, têm-se muito mais opções do que no caso de se ter apenas um *gap* muito largo. Portanto, deve-se considerar, que os casos das figuras 5(e), 5(f) e 5(h) apresentados aqui se saem melhores do que os 3 primeiros analisados, apesar da ótima largura de banda do PBG destes. Todavia, não se pode esquecer que os resultados apresentados aqui consideram somente a propagação dos modos TM. Portanto, para um projeto de estrutura que envolve a propagação de modos TE ou dos modos TE e TM, por exemplo, é necessário ser feito um estudo similar ao feito aqui, considerando desta vez os modos TE. Visto que para uma análise que envolva os dois tipos de propagação, deve-se fazer uma "interseção" de resultados na mesma faixa de freqüência que foi analisada.

AGRADECIMENTOS

Agradecemos todo o suporte e apoio dado pelo DEEC – Departamento de Engenharia Elétrica e de Computação e ao LANE – Laboratório de Análise Numérica em Eletromagnetismo, ambos pertencentes a UFPA – Universidade Federal do Pará, para a realização deste trabalho. Agradecemos também, ao CNPq, que parcialmente custeou este trabalho.

REFERÊNCIAS

[1] J. D. Joannopoulous, R.D. Meade, and J. N. Winn, "*Photonic Crystals"*, Princeton, NJ: Princeton Univ. Press, 1995.

[2] H. G. Park, J. K. Hwang, J. Huh, H.Y. Ryu, Y. H. Lee, J. S. Kim. "Nondegenerate monopole-mode two-dimensional photonic band gap laser". *Appl. Phys. Lett*., vol. 79**,** no. 19, pp. 3032-3034, November 2001.

[3] M. Loncar, T. Yoshie, A. Scherer, P Gogna, Y. Qiu. "Low-threshold photonic crystal laser". *Appl. Phys. Lett.*, vol. 81**,** no. 15, pp. 2680-2682, October 2002.

[4] Y. Hao, C. G. Parini. "Isolation Enhancement of PBG Microstrip Diplexer Patch Antenna". *IEE 11th International Conference on Antennas e Propagation*, 17-20 April 2001.

[5] M. Thèvenot, C. Cheype, A. Reinex and Bernard Jecko. "Directive Photonic-Bandgap Antennas". *IEEE Trans. Microwave Theory and Techniques,'* , Vol. 47, no. 11, pp. 2115-2122, Nov. 1999.

[6] C.L. da S.S. Sobrinho and A.J. Giarola, "Analysis of na optically controlled dielectric waveguide with the use of the FD-FD method, "*Microwave and Optical Technology Letters*, vol. 12, no. 6, pp. 350-353, Aug. 1996.

[7] C.L da S.S. Sobrinho, "Método rigoroso das diferenças finitas em análise de estruturas de guias dielétricos anisotrópicos com perfil de índice de refração variável", Tese de Doutorado, *DMO-FEE-UNICAMP*, Campinas, SP, Julho 1992.

[8] R. V. do Espírito Santo, "Caracterização das Bandas Fotônicas para Estruturas Periódicas 2D constituídas de dielétricos anisotrópicos". Tese de Mestrado, *UFPA/CT/PPGEE*, Belém, PA, Janeiro, 2001.

[9] BALANIS, C. A., *"Advanced Engineering Electromagnetics"*, John Wiley Sons, New York - U.S.A., (1997).

[10] A. Hessel, M.H. Chen, R.C. M. Li, and A.A. Oliner, "Propagation in Periodically Loaded Waveguides with Higher Symmetries", *Proceeding of the IEEE*, vol. 61, no. 2, pp. 183-195, Fev. 1973.

[11] Ishimaru, Akira, *"Electromagnetic Wave Propagation, Radiation and Scattering"*, Prentice Hall, 1991.

[12] Stephen J. Chapman. "*Fortran 90/95 for Scientists and Engineers"*. First edition, WCB-McGraw-Hill: 1998, Singapore.

[13] C. Kittel,"*Introduction Solid State Physics"*, New York: John Wiley, seventh edition, 1996.

[14] N. W. Ashcroft and N. D. Mermin, *"Solid State Physics"*, Cornell University: Saunders Company, 1976.

[15] Yuri M. Galperin, *"Introduction to Modern Solid State Physics"*, Publicação do IOFFE Educational Centre, disponível na *Internet*, através do endereço: http://edu.ioffe.ru/lib/galperin/. Consulta ao site – 25 de Agosto de 2001.

[16] . Hanselman, B. Littlefield. *"MATLAB 5 - versão do estudante, Guia do Usuário"*. Markron Books: 1999, São Paulo, SP.

Carlos Leonidas da Silva Souza Sobrinho realizou a graduação em engenharia elétrica pela Universidade Federal do Pará (UFPA), em 1981. Obteve o título de Mestre, em 1989, pela Universidade Católica do Rio de Janeiro (PUC-RJ), o grau de Doutor pela Universidade de Campinas (UNICAMP), em 1992 e, posteriormente, participou do programa de pós-doutorado no Queen Mary Westfield – University of London, 1999. É professor do departamento de engenharia elétrica da UFPA desde 1986. Atualmente desenvolve pesquisas em: espalhamento eletromagnético e guias de ondas dielétricos com aplicação em bandas de freqüências ópticas e milimétricas, antenas, processamento paralelo, técnicas numéricas, sistemas de aterramento e propagação indoor e outdoor.

Paulo André dos Santos Ramalho realizou a graduação em engenharia elétrica pela Universidade Federal do Pará (UFPA), em 2003. É aluno do Mestrado do PPGEE da UFPA. Atualmente, faz parte do Laboratório de Análise Numérica em Eletromagnetismo (LANE), desenvolvendo pesquisas na área de Estruturas periódicas constituídas de materiais dielétricos, analisando-as, através de uma nova formulação, usando o método FDFD-VETORIAL.

Analysis of an *x*-cut Ti:$LiNbO_3$ Electrooptic Modulator with a Ridge Structure by the Finite Element Method

Nancy M. Abe, Marcos A. R. Franco, Angelo Passaro, and Francisco Sircilli

Instituto de Estudos Avançados – Centro Técnico Aeroespacial – São José dos Campos – SP

***Abstract* — An analysis of a Mach-Zehnder Ti:$LiNbO_3$ traveling-wave electrooptic modulator with a ridge structure is presented in this work. The performance of the device is studied assuming *x*-cut substrate. Two configurations employing ridge structure are compared to a conventional one. This work also presents the influence of some fabrication parameters of the optical waveguide on the factors which evaluates the efficiency of the modulators. The characteristics of both the optical waveguide and the coplanar waveguide electrode are computed applying the scalar finite element method.**

***Index terms* — integrated optics, optical waveguides, coplanar waveguides, ridge waveguides, electrooptic modulation, finite element method**.

I. Introduction

Electrooptic modulators have widespread use in optical communication systems, optical signal processing, and optical computing. In recent years, several modulators structures have been investigated to achieve large modulation bandwidth with a low driving voltage. The coplanar waveguide shape, the introduction of buffer layers, the reduction of the substrate thickness, and shielding planes are some of the characteristics that can be introduced and optimized in order to improve the modulators performance [1]-[8].

This work presents an analysis of a Ti:$LiNbO_3$ traveling-wave electrooptic modulator employing a ridge structure. The study focuses on the lossless device behavior assuming an *x*-cut substrate. Two ridge structure configurations are compared to a conventional one. An analysis of the influence of some optical waveguide fabrication parameters, such as the diffusion temperature and the width of the titanium strip, on the efficiency of the modulators is also presented.

The Finite Element Method (FEM) was applied to analyze the microwave and the optical propagation properties. The microwave electric field was computed by applying the quasi-TEM approximation and the optical propagation properties were computed from the scalar wave equation.

II. The Finite Element Formulations

A. Quasi-Static Analysis – TEM Modes

The quasi-TEM modes are related to the solutions of the Laplace equation for the electric potential ϕ:

$$\nabla \cdot \left(\bar{\varepsilon}_r \ \nabla \phi \right) = 0 , \tag{1}$$

where the relative permittivity tensor is given by:

$$\bar{\varepsilon}_r = \begin{bmatrix} \varepsilon_{xx} & 0 \\ 0 & \varepsilon_{yy} \end{bmatrix} \tag{2}$$

The finite element method applied to (1) yields the matrix equation

$$[S]\{\phi\}^T = \{b\}^T , \tag{3}$$

where:

$$[S] = \int_{\Omega} \left(\varepsilon_{xx} \ \{N\}_x^T \ \{N\}_x + \varepsilon_{yy} \{N\}_y^T \ \{N\}_y \right) dx dy , \tag{4}$$

$$\phi = \{N\}\{\phi\}^T ,$$

$$\vec{E} = - \nabla \phi ,$$

{ } represents a row matrix, { }^{T} stands for a transposed matrix and $\{N\}$ represents a complete set of base functions for the used finite elements. $\{N\}_x$ and $\{N\}_y$ represent the partial derivative of the base functions in *x* and *y*, respectively.

B. Optical Modes

The modal analysis of the Ti:$LiNbO_3$ waveguide was carried out by a scalar finite element implementation for both nonhomogeneous and anisotropic media [9], [10].

The Helmholtz equation in the scalar approximation, for a lossless, nonhomogeneous and anisotropic dielectric optical waveguide with diagonal relative permittivity tensor, and a harmonic *z*-propagating wave, can be expressed for the E^x modes as

$$\begin{aligned} & n_z^2 \frac{\partial}{\partial x}\left(\frac{1}{n_z^2} \right) \frac{\partial \left(n_x^2 E_x \right)}{\partial x} + \frac{\partial^2 \left(n_x^2 E_x \right)}{\partial x^2} \\ & + n_z^2 \frac{\partial^2 E_x}{\partial y^2} + k_0^2 \, n_x^2 \, n_z^2 \, E_x = n_z^2 \beta^2 E_x , \end{aligned} \tag{5}$$

and for the E^y modes as follows

$$\begin{aligned} & \frac{\partial^2 H_x}{\partial x^2} + n_y^2 \frac{\partial}{\partial y}\left(\frac{1}{n_z^2} \frac{\partial H_x}{\partial y} \right) \\ & + n_y^2 k_0^2 H_x = \beta^2 H_x \end{aligned} \tag{6}$$

where k_0 is the free space wavenumber and β is the propagation constant. The variables $n_x(x,y)$ and $n_y(x,y)$ are the refractive indexes in the transversal x and y directions

respectively, and $n_z(x,y)$ is the refractive index in the longitudinal direction.

The application of the Weighted Residual Method with the Galerkin Approximation in (5) and (6) yields the matrix equation

$$[F]\{\phi\}^T = n_{eff}^2\,[M]\{\phi\}^T, \tag{7}$$

where $n_{eff} = \beta / k_0$ is the effective index [9]-[11]. The matrices for each finite element are given by:

$$[M] = \int_{\Omega} \boldsymbol{A}\; k_0^2\; \{N\}^T \{N\}\, dx\, dy, \tag{8}$$

$$[F] = [F_1] - [F_2]. \tag{9}$$

The parameter $\boldsymbol{A}$ and the matrices $[F_1]$ and $[F_2]$ depend on the propagation modes.

For the E^x modes $\boldsymbol{A} = n_z^2$ and the matrices are:

$$[F_1] = \int_{\Omega} \left(k_0^2\, n_x^2\, n_z^2\, \{N\}^T \{N\} - n_x^2\, \{N\}_x^T \{N\}_x\right) dx\, dy - \int_{\Omega} n_z^2\, \{N\}_y^T \{N\}_y\; dx\, dy \tag{10}$$

and

$$[F_2] = \int_{\Omega} \left(\delta_x \frac{\partial n_x^2}{\partial x} \{N\}_x^T \{N\} + \delta_z \frac{\partial n_z^2}{\partial y} \{N\}^T \{N\}_y \right) dx\, dy - \int_{\Omega} \delta_z \{N\}^T n_z^2\; \frac{\partial g_z^2}{\partial x} \left(\delta_x \frac{\partial n_x^2}{\partial x} \{N\} + n_x^2\, \{N\}_x \right) dx\, dy \tag{11}$$

For E^y modes $\boldsymbol{A} = 1$,

$$[F_1] = \int_{\Omega} \left[k_0^2\, n_y^2\; \{N\}^T \{N\} - \{N\}_x^T \{N\}_x \right] dx\, dy - \int_{\Omega} n_y^2\, g_z^2\, \{N\}_y^T \{N\}_y\; dx\, dy \tag{12}$$

and

$$[F_2] = -\int_{\Omega} \delta_y\; g_z^2\, \frac{\partial n_y^2}{\partial y}\; \{N\}^T\; \{N\}_y\, dx\; dy - \int_{\Omega} \delta_z\; n_y^2 \left(\frac{\partial g_z^2}{\partial y} + g_z^4\, \frac{\partial n_z^2}{\partial y} \right) \{N\}^T\; \{N\}_y\, dx\; dy\;, \tag{13}$$

For both propagation modes $g_z = 1/n_z$. The parameters δ_x and δ_z assume either the value 1 for diffused index in the x and z directions respectively, or zero for constant index. The matrix $[F_2]$ is sparse and nonsymmetrical because of the presence of terms with partial derivative of the refractive index.

In this work, the variation of the refractive indexes and their spatial derivatives inside each finite element are expanded in terms of the first order Lagrange type base functions $\{N\}$:

$$n_i^2 = \{N\}\{n_i^2\}^T, \quad i, j = x, y, z$$

$$\frac{\partial n_i^2}{\partial j} = \{N\}_j \{n_i^2\}, \qquad \frac{\partial g_z^2}{\partial j} = \{N\}_j \{g_z^2\}$$

III. Ti:LiNbO$_3$ Channel Optical Waveguide

The effect of the following manufacturing parameters are considered to define the optical channel waveguide: the initial width of the Ti strip, W, the initial thickness of the Ti strip, H, the ion diffusion temperature, T, and the ion diffusion time, t. Additionally, the parameters were chosen to guarantee the complete diffusion of Ti into the $LiNbO_3$ substrate avoiding the presence of residual titanium oxide films which cause scattering losses and increase insertion loss.

For Ti:$LiNbO_3$ channel waveguides, the refractive index in the diffused region follows [14]:

$$n_{e,o}^2(x,y,\lambda) = n_{b_{e,o}}^2 + \left[\left(n_{b_{e,o}} + \Delta n_{s_{e,o}} \right)^2 - n_{b_{e,o}}^2 \right] exp\left(-\frac{y^2}{d_y^2} \right) f\left(\frac{2x}{W} \right), \tag{14}$$

where:

$$f\left(\frac{2x}{W}\right) = \frac{1}{2}\left\{ erf\left[\frac{W}{2d_x}\left(1 + \frac{2x}{W}\right)\right] + erf\left[\frac{W}{2d_x}\left(1 - \frac{2x}{W}\right)\right]\right\},$$

e and o denote the extraordinary and ordinary principal crystal axes respectively, x and y are the coordinates of a point in the substrate, d_x and d_y are the diffusion width and depth respectively, n_b is the substrate refractive index and Δn_s stands for the variation of the surface index with the wavelength.

In addition, $\Delta n_{se,o}$ is given in terms of H and some additional fitting parameters [12] :

$$\Delta n_{s_{e,o}}(\lambda) = \left[B_0(\lambda) + B_1(\lambda) \frac{H}{d_{y_{e,o}}} \right] \left(\frac{H}{d_{y_{e,o}}} \right)^{\alpha_{e,o}}, \tag{15}$$

$$\alpha_e = 0.83, \quad \alpha_o = 0.53, \quad 0.6 \le \lambda(\mu m) \le 1.6$$

$$B_{0e}(\lambda) = 0.385 - 0.430\lambda + 0.171\lambda^2,$$

$$B_{1e}(\lambda) = 9.130 + 3.850\lambda - 2.490\lambda^2,$$

$$B_{0o}(\lambda) = 0.0653 - 0.0315\lambda + 0.0071\lambda^2,$$

$$B_{1o}(\lambda) = 0.4780 + 0.4640\lambda - 0.3480\lambda^2.$$

The diffusion coefficients D_x and D_y, the diffusion width d_x and depth d_y and the depth of refractive index change profiles d_{ye} and d_{yo} can be calculated by the Arrhenius Law:

$$D_i = D_{i0}\, exp\left(-E_{i0} / kT \right), \quad i = x, y \tag{16}$$

$$d_i = 2\sqrt{D_i\, t}\;, \quad i = x, y \tag{17}$$

$$d_{y_{e,o}} = \frac{d_y}{\sqrt{\alpha_{e,o}}}, \quad (18)$$

where D_{i0} is the diffusion constant, E_{i0} is the activation energy and k is the Boltzmann constant. The constants for Ti-diffused $LiNbO_3$ are presented in Table I [12].

Table 1.Coefficients of the Arrhenius Law for Ti:$LiNbO_3$ Guides.

D_{x0} (μm^2 / h)	5.0 e+9
D_{y0}(μm^2 / h)	1.35 e+8
E_{x0} (eV)	2.60
E_{y0} (eV)	2.22

The refractive indexes dispersion of the SiO_2 and of the $LiNbO_3$ are taken into account by using the three-terms Sellmeier equation for SiO_2 and the equivalent relations for $LiNbO_3$ presented in [11].

IV. ANALYSIS

The cross-sectional view of the analyzed structure is shown in Fig.1 The magnified region shows geometrical details of the ridge. The buffer layer thickness d on the horizontal plane is larger than the thickness b along the side wall. This difference results from the fabrication process. The design and fabrication techniques of an optical modulator with this kind of structure are described in [4], for a z-cut $LiNbO_3$ substrate.

The numerical analysis was performed for a wavelength of 1.523 μm considering the geometry shown in Fig.1. The inclination α of the ridge side walls is assumed equal to 70º, compatible with the values obtained in experimental measurements [4]. The ridge height h and the electrode gap g are assumed to be 3.5 μm and 15 μm, respectively. The guide is built in a x-cut $LiNbO_3$ substrate.

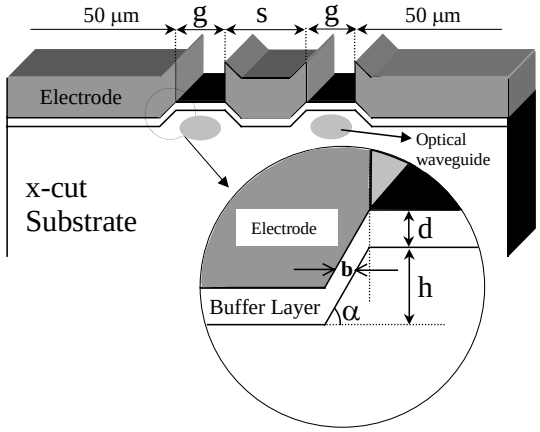

Fig. 1. The cross-sectional view of the Ti:$LiNbO_3$ Mach-Zehnder traveling-wave electrooptic modulator employing a ridge structure and a detail of the ridge.

The half-wave voltage, the driving power, the characteristic impedance, the microwave effective index, the overlap integral and the modulation bandwidth are used to evaluate the optical modulators performance. The microwave effective index and the characteristic impedance are given by [3]:

$$N_{eff} = \sqrt{\frac{C}{C_o}} \quad (19)$$

$$Z_c = \frac{1}{c\sqrt{C_o C}} \quad (20)$$

where c is the velocity of light in vacuum, C and C_0 are the capacitance per unit length of the CPW when the dielectric material is considered and when it is replaced by vacuum, respectively.

The modulation-frequency bandwidth Δf for the lossless traveling-wave modulators is given by [13]:

$$\Delta f = \frac{1.4\ c}{\pi \left| N_{eff} - n_{eff} \right| L} \quad (21)$$

where L is the interaction length, n_{eff} and N_{eff} are the effective index for the optical and the quasi-TEM modes, respectively.

The overlap integral factor Γ, for each optical waveguide, the half-wave voltage V_π and the driving power modulation P_{in}, are calculated as follows [3], [6]:

$$\Gamma = \frac{g}{V} \frac{\iint E_{op}^2(x,y)\, E_{TEM}(x,y)\, dxdy}{E_{op}^2(x,y)\, dxdy} \quad (22)$$

$$V_\pi = \frac{\lambda_o\, g}{n_e^3 r_{33} \left(\left|\Gamma_1\right| + \left|\Gamma_2\right| \right) L} \quad (23)$$

$$P_{in} = \frac{V_\pi^2}{8 Z_s \left[1 - \left(\frac{Z_s - Z_c}{Z_s + Z_c} \right)^2 \right]} \quad (24)$$

where g is the gap between the electrodes (Fig. 1), V is the applied voltage, E_{op} is the optical electric field, E_{TEM} is the component of the microwave electric field, λ_o is the free space optical wavelength, n_e is the extraordinary refractive index of the substrate, r_{33} is the electrooptic coefficient of $LiNbO_3$, Γ_1 and Γ_2 are the overlap integral factors for each one of the optical guides of the modulator and Z_s is the impedance of the microwave source. For x-cut Ti:$LiNbO_3$ waveguides symmetrically positioned in relation of the central electrode, $|\Gamma| = |\Gamma_1| = |\Gamma_2|$.

A. Variation of the Electrode Thickness

Three configurations were considered to perform this analysis. Two of them employ ridge structures, as shown in Fig.1, and the other one has conventional characteristics - i.e. it presents rectangular shaped electrodes and the interface between the buffer layer and the substrate is a plane that is represented by a straight line for a 2D analysis. The width of the central electrode and the thickness of the buffer layer for these configurations are shown in Table I.

The fabrication conditions of the optical waveguide for the results presented in this section are 3 hours of

diffusion time at 1050 °C and initial Ti strip width and thickness of 5 μm and 80 nm, respectively [9], [14].

Table 2. Electrode width and buffer layer thickness

Configuration		Central electrode width s (μm)	Buffer layer thickness d (μm)
A	Ridge	5	2.5
B	Ridge	8	1.5
C	Conventional	8	1.5

For the studied configurations, both the electrical effective index N_{eff} and the characteristic impedance Z_c are shown in Fig. 2 as a function of the electrode thickness.

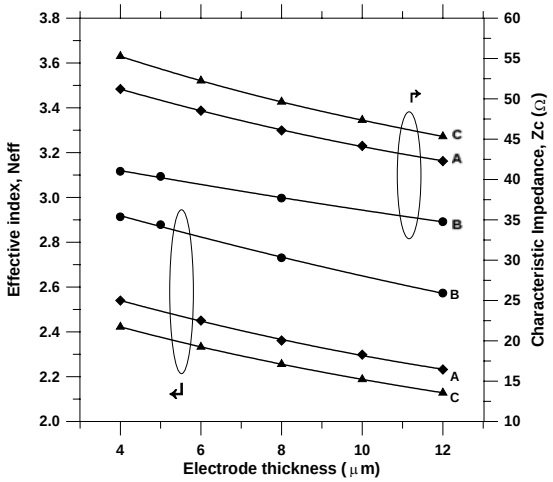

Fig. 2. Effective index N_{eff} and characteristic impedance Z_c as a function of the electrode thickness, for the configurations A, B and C of Table 2.

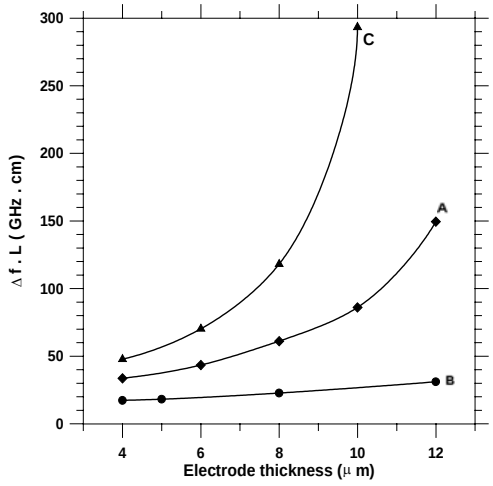

Fig. 3. $\Delta f\, L$ product as a function of the electrode thickness, for the configurations A, B and C.

The behavior of the product $\Delta f\, L$ is shown in Fig. 3 while Fig. 4 shows the variation of the products $V_\pi L$ and $P_{in} L^2$. In this analysis, it was assumed impedance Z_s of 50 Ω and the microwave losses were not considered. The configurations A and C provide better characteristics for impedance and velocity matching conditions while configurations A and B (ridge structure) present lower values of the product $V_\pi L$.

The configuration B presents the lowest modulation bandwidth but it presents the smallest driving power values for a given electrode length. Additionally, as the influence of the electrode thickness on parameters Δf, V_π and P_{in} is small, the control on the electrodes deposition process would not need to be too rigorous for this configuration.

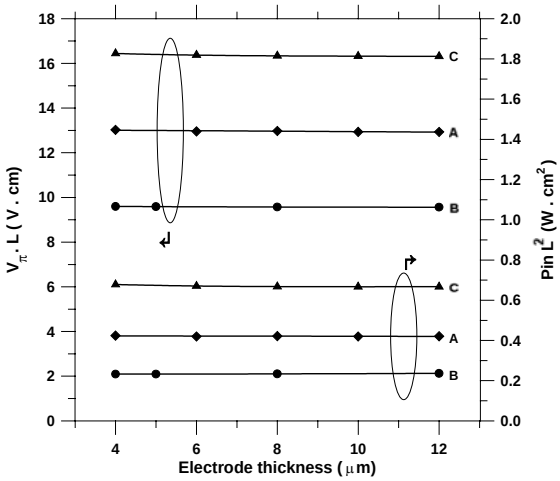

Fig. 4. $V_\pi L$ product and $P_{in} L^2$ product as a function of the electrode thickness, for the configurations A, B and C.

B. Variation of the Buffer Layer Thickness

The results presented in this section correspond to the configurations A and B, assuming the electrodes thickness of 8 μm and 4 μm, respectively. The same optical waveguide fabrication parameters described in section *A* were used. The electrical effective index N_{eff} and the characteristic impedance Z_c are shown in Fig. 5 as a function of the buffer layer thickness. The product $\Delta f\, L$ is shown in Fig. 6 and the overlap integral factor is presented in Fig. 7. The products $V_\pi L$ and $P_{in} L^2$ are shown in Fig. 8.

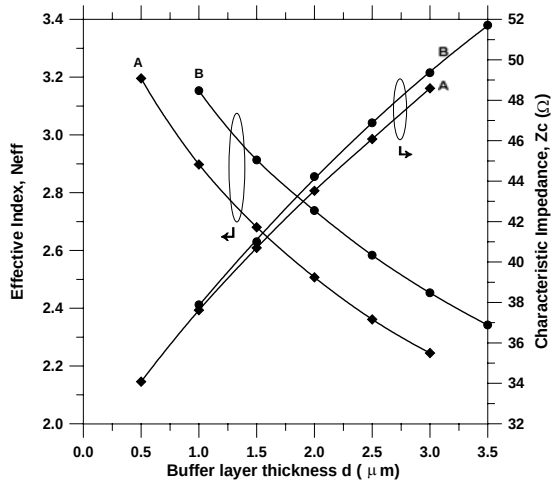

Fig. 5. Effective index N_{eff} and characteristic impedance Z_c as a function of the buffer layer thickness, for both configurations A and B.

The driving power for the configuration B (Fig. 8) reaches approximately the same value of the one obtained for the conventional configuration (Fig. 4), when the buffer layer thickness d equals to the ridge height h = 3.5 μm. We should remember, however, that the buffer layer thickness of the configuration C for the results presented in Fig. 4 is 1.5 μm.

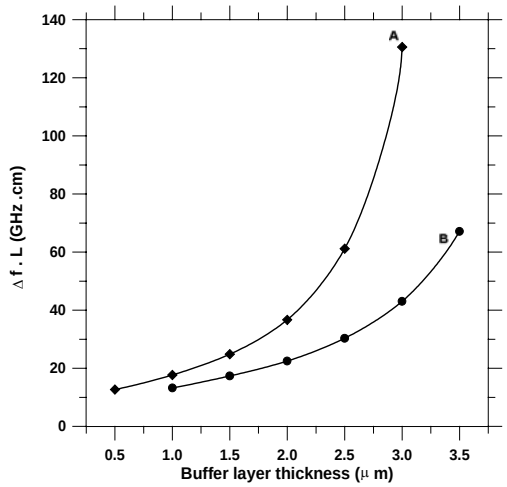

Fig. 6. $\Delta f L$ product of the modulation-frequency bandwidth and the interaction length as a function of buffer layer thickness, for both configurations A and B.

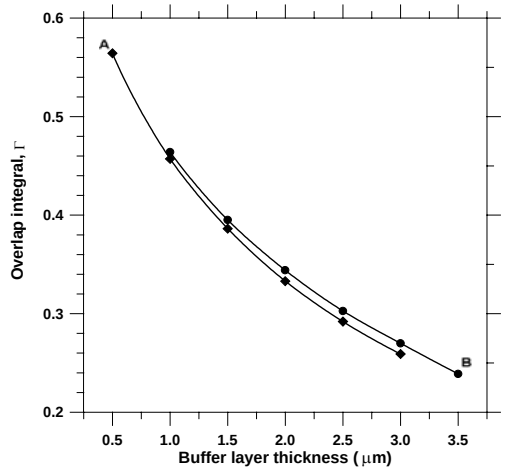

Fig. 7. Overlap integral factor as a function of the buffer layer thickness, for both configurations A and B.

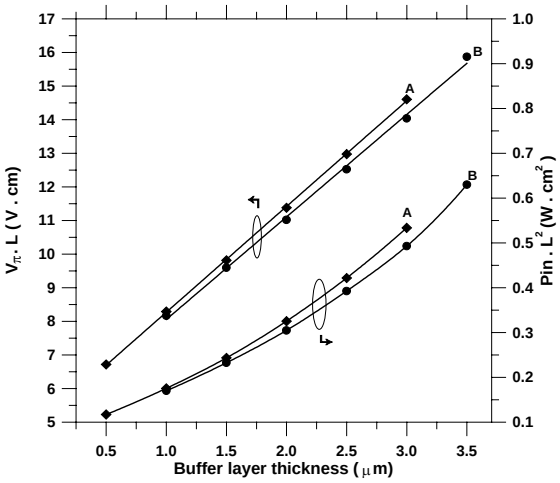

Fig. 8. $V_\pi L$ and $P_{in} L^2$ products as functions of the buffer layer thickness, for both A and B configurations.

C. Variation of the Optical Waveguide Fabrication Conditions

In this section, the behavior of the modulator is presented as a function of some of the optical waveguide fabrication conditions, namely, the diffusion temperature, the diffusion time and the initial Ti strip width. For this purpose, the configuration A with an electrode thickness of 8 μm has been adopted.

The optical mode profiles in the diffused region were calculated following the method presented in [9], [10], [14]. This method is suitable for computing the optical mode profiles for the ridge structure waveguide since the Ti diffusion is carried out before the etching procedure. Otherwise, the geometry of the substrate could affect the Ti diffusion.

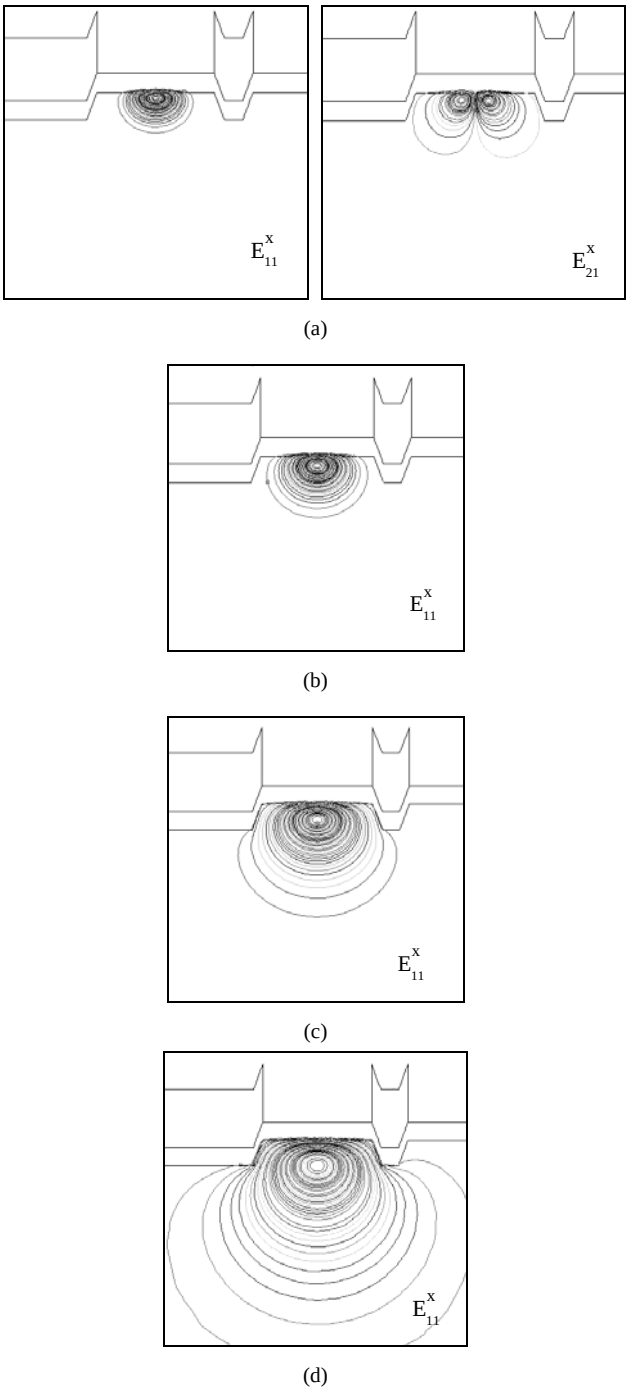

Fig. 9. Evolution of the optical mode profile as a function of the diffusion temperature (a) 1000 °C, (b) 1050 °C, (c) 1100 °C and (d) 1150 °C.

A symmetric Gaussian function and a Hermite-Gaussian trial solution are often used to approximately represent the fundamental mode profile in weakly guiding

optical waveguides . However, to use these functions the optical mode sizes should be known. As the mode sizes depend on the fabrication parameters, they need to be determined *a priori* either by empirical means or by some other technique. Moreover, these approximations should not provide accurate optical field profiles for waveguides built in complex geometric structures. The application of numerical analysis, like the one adopted in this work, allows obtaining careful descriptions of the mode profiles.

Fig. 9 shows the evolution of the optical modes profile (optical spots) as a function of the diffusion temperature, assuming 5 μm and 80 nm of initial Ti strip width and thickness, respectively, and 3 h of diffusion time. Under these fabrication conditions, the obtained results showed that the monomode operation for E^x modes is reached for temperatures higher than 1000 °C, Fig. 10.

The products $V_\pi L$ and $P_{in} L^2$ as a function of the diffusion temperature are shown in Fig. 11. As the diffusion temperature increases, the fundamental optical mode spreads out through the substrate. This leads to a decrease of the overlap integral and both the $V_\pi L$ and $P_{in} L^2$ products increase.

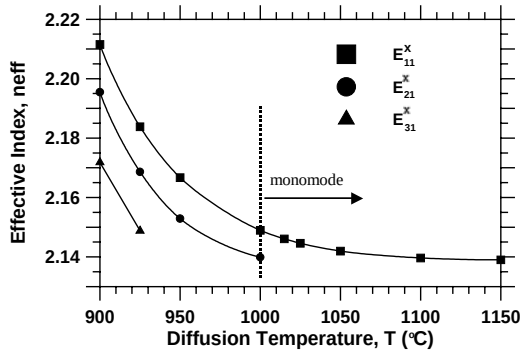

Fig. 10. Effective index for the three first optical modes as a function of the Ti-layer diffusion-process temperature.

Notice that mode profiles resembling that presented in Fig. 9(d), can occur for temperatures lower than 1150 °C. Other fabrication conditions or different geometric parameters, such as a small electrode gap, can lead to a similar behavior.

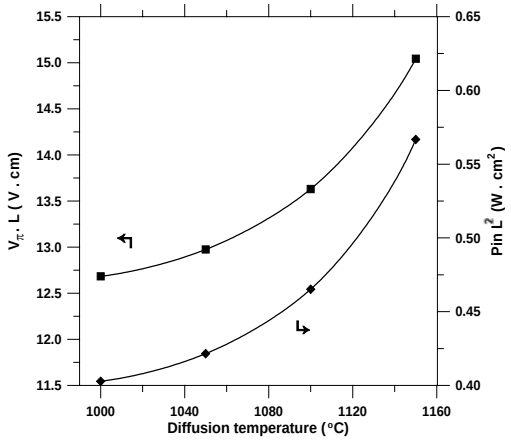

Fig. 11. $V_\pi L$ product and $P_{in} L^2$ product as a function of the diffusion temperature.

$V_\pi L$ and $P_{in} L^2$ products are shown in Fig. 12 as a function of the diffusion time for a initial Ti strip width and thickness of 5 μm and 80 nm, respectively. If the diffusion is carried out for a long time, the working characteristics of the modulator become worse, although the waveguide keeps on monomode condition.

Fig. 13 shows the products $V_\pi L$ and $P_{in} L^2$ as a function of the initial Ti strip width for a diffusion time of 3 h at 1050 °C and 80 nm of Ti strip thickness. The half-wave voltage and the driving modulation power decrease slightly as the initial Ti strip width increases. However, the monomode operation is achieved for Ti strip widths smaller than 7 μm (Fig. 14).

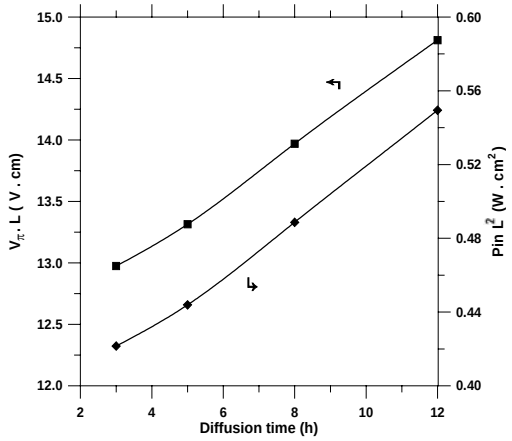

Fig. 12 - $V_\pi L$ product and $P_{in} L^2$ product as a function of the diffusion time.

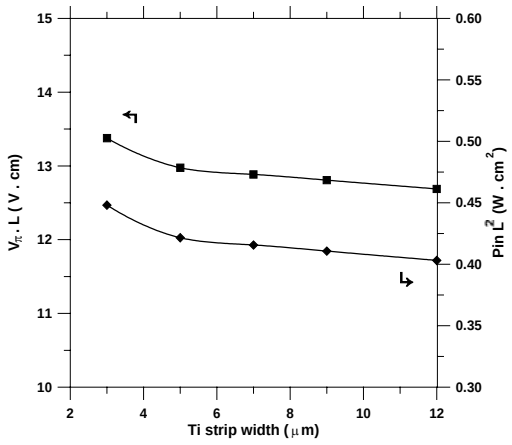

Fig. 13. $V_\pi L$ product and $P_{in} L^2$ product as a function of the initial Ti strip width.

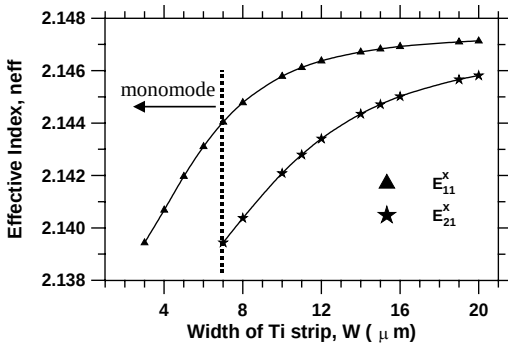

Fig. 14. Effective index as a function of the initial width of Ti strip.

V. CONCLUSION

A scalar FEM formulation was applied to compute both the traveling-wave electrical characteristics and the optical waveguide propagation properties of a x-cut Ti:$LiNbO_3$ electrooptic modulator with a ridge structure. Two configurations employing ridge structure were compared to a conventional one. The study also included a numerical analysis of the electrooptic modulator behavior as a function of the fabrication parameters of the optical waveguide.

The analyzed modulators employing ridge structure can provide lower power consumption than the conventional one does. However, the velocity mismatch debases their wide-band applications. Even so, profitable operation conditions were established for this kind of modulators. One of the studied configurations reduces substantially the microwave driving power with a $V_\pi L$ product lower than 10 V.cm at a $\Delta f L \cong 20$ GHz.cm condition. The other one can be used in applications that require larger modulation bandwidth ($\Delta f L \cong 60$ GHz.cm for an electrode thickness of 8 μm) but with a $V_\pi L$ product of 13 V.cm.

ACKNOWLEDGEMENTS

The authors wish to thank FAPESP for partial financial support of this work (proc. 98/07789-7).

REFERENCES

[1] H. Jin, M. Bèlanger and Z. Jakubczyk, "General Analysis of Electrodes in Integrated-Optics Electrooptic Devices", *IEEE Journal of Quantum Electronics*, vol. 27, No. 2, pp. 243-251, Feb. 1991.

[2] K. Kawano, "High-Speed Shielded Velocity-Matched Ti:$LiNbO_3$ Optical Modulator", *IEEE Journal of Quantum Electronics*, vol. 29, No. 9, pp. 2466-2475, Sept. 1993.

[3] X. Zhang and T. Miyoshi, "Optimum Design of Coplanar Waveguide for $LiNbO_3$ Optical Modulator", *IEEE Transactions on Microwave Theory and Techniques*, vol. 43, No. 3, pp. 523-528, March 1995.

[4] K. Noguchi, O. Mitomi, H. Miyazawa and S. Seki, "A Broadband Ti:$LiNbO_3$ Optical Modulator with a Ridge Structure", *Journal of Lightwave Technology*, vol. 13, No.6 , pp. 1164-1168, June 1995.

[5] N. H. Zhu, E. Y. B. Pun and P. S. Chung, "Analysis of Shielded Coplanar Waveguide with Trapezoidal Electrodes", *IEEE Photonics Technology Letters*, vol. 8, No. 2, pp. 242-244, Feb. 1996.

[6] K. W. Hui, K. S. Chiang, B. Wu and Z. H. Zhang, "Electrode Optimization for High-Speed Traveling-Wave Integrated Optic Modulators", *Journal of Lightwave Technology*, vol. 16, No. 2, pp. 232-238, Feb. 1998.

[7] M. Koshiba, Y. Tsuji and M. Nishio, "Finite Element Modeling of Broad-Band Travelling-Wave Optical Modulators," *IEEE Transactions on Microwave Theory and Techniques*, vol.47, No.9, pp. 1627-1633, Sept. 1999.

I.-L. Gheroma, P. Savi, and R.M. Osgood, Jr., "Thin Layer Design of X-Cut $LiNbO_3$ Modulators," *IEEE Photonics Technology Letters*, vol. 12, No. 12, pp. 1618-1620, Dec. 2000.

[9] M. A. R. Franco, A. Passaro, J. R. Cardoso, and J. M. Machado, "Finite Element Analysis of Anisotropic Optical Waveguide with Arbitrary Index Profile", *IEEE Transactions on Magnetics*, vol.35, No.3, pp.1546-1549, May 1999.

[10] M. A. R. Franco, A. Passaro, F. Sircilli Neto, J. R. Cardoso, and J. M. Machado, "Modal Analysis of Anisotropic Diffused-Channel Waveguide by a Scalar Finite Element Method", *IEEE Transactions on Magnetics*, vol. 34, No. 5, pp.2783-2786, Sept. 1998.

[11] M. Koshiba, *Optical Waveguide Theory by the Finite Element Method*, 1st ed., KTK Scientific Publishers/Kluwer Academic Publishers, Tokyo/Dordrecht, The Netherlands, 1992.

[12] S. Fouchet, A. Carenco, C. Daguet, R. Guglielmi, and L. Riviere, "Wavelength Dispersion of Ti Induced Refractive Index Change in $LiNbO_3$ as a Function of Diffusion Parameters," *J. Lightwave Technol.*, vol. LT-5, N. 5, pp. 700-708, May 1987.

[13] H. Nishihara, M. Haruna, and T. Suhara, *Optical Integrated Circuits*, 1st ed., McGraw-Hill, 1989, pp.109-111.

[14] D. Zhang, C. Chen, J. Li, G. Ding, X. Chen, and Y. Cui, "A Theoretical Study of a Ti-Diffused Er:$LiNbO_3$ Waveguide Laser," *IEEE Journal of Quantum Electronics*, vol. 32, No. 10, pp. 1833-1838, Oct. 1996.

Nancy Mieko Abe obtained the B.Sc. and M.Sc. degrees in electrical engineering from the Escola Politécnica da Universidade de São Paulo (EPUSP), Brazil, in 1989 and 1992, respectively. In 1997, she obtained the doctorate degree in electrical engineering from the same university (EPUSP). In 1998, she joined the Institute for Advanced Studies of Aerospace Technical Center (IEAv-CTA), Brazil, as a researcher fellow. Since 2002 she is an Adjunct Researcher in the Virtual Engineering Laboratory of IEAv/CTA. Her research interests include electromagnetic field computation, heat conduction analysis, plasma simulation, numerical methods and high-performance parallel programming.
(email: nancy@ieav.cta.br)

Marcos Antonio Ruggieri Franco was graduated in Physics at Pontifícia Universidade Católica de São Paulo – Brazil (PUC-SP), in 1983. In 1991, he finished his Master of Science degree in Nuclear Physics at Intituto de Física da Universidade de São Paulo-Braxil (IFUSP). In 1999, he received his doctorate in Electrical Engineering from the Escola Politécnica da Universidade de São Paulo – Brazil (POLI-USP). In 1987, he joined the research team of the division of Applied Physics at Institute for Advanced Studies (IEAv) at Dentro Técnico Aeroespacial (CTA). Since 2001, he is also associated professor of the pos-graduate course of Electronic Computation Engineering from the Instituto Tecnológico de Aeronáutica (ITA). His major areas of interest are the application of the Finite Element Method for the design of electromagnetic devices sucha as microwave and optical waveguides, fiber optics, integrated optics, antennas and electromagnetic scattering problems.
(email: marcos@ieav.cta.br)

Angelo Passaro received the B.Sc. in physics (1981) and the M.Sc degrees in nuclear physics (1988) from the Instituto de Física da Universidade de São Paulo (IFUSP), Brazil. In 1998, he completed his doctorate degree in electrical engineering at the Escola Politécnica da Universidade de São Paulo (EPUSP), Brazil. In 1984, he joined the Institute for Advanced Studies of Aerospace Technical Center. Since 1999, he has been the head of the Virtual Engineering Laboratory of (IEAv-CTA). His current research interests are in high-performance parallel programming, numerical methods, electromagnetic field computation, plasma simulation, and heat conduction analysis.
(email:angelo@ieav.cta.br)

Francisco Sircilli Neto was graduated at the Institute of Physics of São Paulo University (IFUSP), Brazil, in 1981. His Master Science was obtained in 1986 at the National Institute for Space Research (INPE), Brazil, in the area of Nuclear Geophysics. In 1997 he concluded his Doctorate in Electrical Engineering at the Polytechnic School of São Paulo University (POLI-USP), Brazil. Since 1985 he joined the research team of Division of Applied Physics of the Institute for Advanced Studies of the Aerospace Technical Center (IEAv/CTA). Today his main area of interest is the application of the Finite Element Method (FEM) to wave propagation in devices such as microwave, optical waveguides and fiber optics, as well as to antennas and electromagnetic scattering problems.
(email: sircilli@ieav.cta.br)

A Finite Element Analysis of a Ti:$LiNbO_3$ Traveling-Wave Electrooptic Modulator with Floating Electrodes

Marcos A. R. Franco, Angelo Passaro, Nancy M. Abe, José M. Machado* and Francisco Sircilli

Instituto de Estudos Avançados – Centro Técnico Aeroespacial – São José dos Campos – SP
* IBILCE – UNESP – São José do Rio Preto - SP

***Abstract* — This work presents a quasi-static analysis of an *x*-cut Mach-Zehnder-like modulator which includes a set of floating electrodes. The results are compared to the ones obtained for a modulator of conventional electrode configuration. The electrooptic modulators were analyzed by using the finite element method. The numerical results complement information presented previously in literature.**

***Index terms* — integrated optics, optical waveguides, coplanar waveguides, electrooptic modulation, finite element methods.**

I. INTRODUCTION

Electrooptic modulators with traveling-wave (TW) electrodes are one of the most important wideband devices for optical communication systems, high precision sensors, optical signal processing and optical computing. The development of technologies for the design and construction of wideband and lower power consumption modulators has demanded great efforts in the last years [1]-[8]. Particularly, our research group is engaged in the development of software systems for the analysis and design optimization of integrated optic devices and components. The analyses comprehend the influence of constructive parameters, such as, time and temperature of the ion diffusion process, different geometric configurations and materials. Results presented in literature are used regularly for the evaluation of both the adequacy of the models we adopt and the software solutions we develop.

In this work, an *x*-cut Mach-Zehnder modulator with TW electrodes and a set of extra floating electrodes is analyzed. The inclusion of the floating electrodes was proposed in [1] for an *x*-cut $LiNbO_3$ substrate, in order to increase the microwave field in the electrooptic interaction region. These floating electrodes are located between the $LiNbO_3$ substrate and the buffer layer, Fig. 1.

Both the microwave electric field and the optic field were computed in this work by applying the Finite Element Method (FEM).

The effects of the geometric parameters *G*, *g*' and *b* (Fig. 1) on the modulator performance are analyzed in order to improve the design. The results are compared to the ones obtained for a conventional *x*-cut Mach-Zehnder modulator with the same geometric characteristics.

II. THE MODEL

The Mach-Zehnder modulator manufactured with coplanar waveguides (CPW) transmission lines can be characterized by the following electrical parameters: the characteristic impedance Z_c, the effective index N_{eff} of the transverse electromagnetic (TEM) mode, the bandwidth Δf, the overlap integral factor Γ of each optical waveguide, the half-wave voltage V_π and the microwave driving power P_{in}. These parameters are defined as follows [3]-[5], [9]:

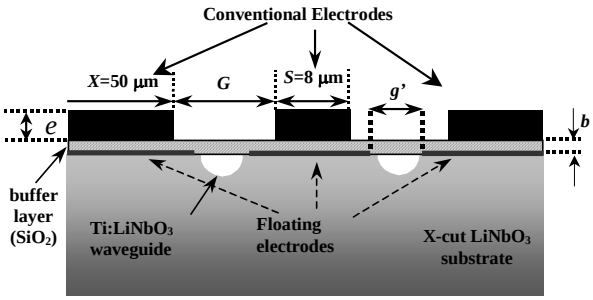

Fig. 1. *Cross-section view of the x-cut Mach-Zehnder optical modulator with a set of extra floating electrodes.*

$$Z_c = \frac{1}{c}\frac{1}{\sqrt{CC_1}}, \tag{1}$$

$$N_{eff} = \sqrt{\varepsilon_{eff}} = \sqrt{\frac{C}{C_1}}\ , \tag{2}$$

$$\Delta f\ L = \frac{1.4\,c}{\pi\left|\sqrt{\varepsilon_{eff}} - n_{eff}\right|} \tag{3}$$

$$\Gamma = \frac{G}{V}\frac{\iint E_{op}^2(x,y)E_{el}(x,y)\,dxdy}{\iint E_{op}^2(x,y)\,dxdy} \tag{4}$$

$$V_\pi\ L = \frac{\lambda_0\ G}{n_{be}^3\ r_{33}\left(|\Gamma_1| + |\Gamma_2|\right)} \tag{5}$$

$$P_{in} = \frac{V_\pi^2}{8Z_s\left[1-((Z_s - Z_c)/(Z_s + Z_c))^2\right]}. \tag{6}$$

In (1)-(6), *C* is the capacitance per unit length of the CPW with the usual materials, C_1 is the capacitance per unit length of the CPW in vacuum, *c* is the free-space light velocity, n_{eff} is the effective index of the optical wave, *V* is the static voltage between the electrodes, E_{op} is the optical electric field, E_{el} is the electric field of the

TEM wave (E_x component for the *x*-cut case), L is the length of the CPW electrodes, λ_0 is the free-space optical wavelength, n_{be} is the extraordinary refractive index of the substrate at λ_0, r_{33} is the electrooptic coefficient of $LiNbO_3$ and Z_s is the impedance of the microwave source. Notice that, for *x*-cut Mach-Zehnder modulators with optical waveguides positioned in the middle of the gap G, Fig. 1, the overlap integral for both optical waveguides, $|\Gamma_1|$ and $|\Gamma_2|$, are identical, i.e. $|\Gamma| = |\Gamma_1| = |\Gamma_2|$.

In this work, E_{el} is computed by the FEM in the quasi-static approximation (TEM modes), as follows.

The TEM modes are related to the solutions of the Laplace equation for the electric potential ϕ:

$$\nabla\cdot(\bar{\varepsilon}_r \nabla\phi) = 0, \tag{7}$$

where the diagonal relative permittivity tensor is given by:

$$\bar{\varepsilon}_r = \begin{bmatrix} \varepsilon_{xx} & 0 \\ 0 & \varepsilon_{yy} \end{bmatrix}. \tag{8}$$

The FEM applied to (7) yields the matrix equation:

$$[S]\,\{\phi\}^T = \{0\}^T \ , \tag{9}$$

where :

$$[S] = \int_\Omega \left(\varepsilon_{xx} \{N\}_x^T \{N\}_x + \varepsilon_{yy} \{N\}_y^T \{N\}_y \right) dx\, dy \ , \tag{10}$$

$$\phi = \{N\}\{\phi\}^T \text{, and } \ \vec{E} = -\nabla\phi \ ,$$

{ } represents a row matrix, { }^{T} stands for a transposed matrix and {N} represents a complete set of base functions for the used finite elements. $\{N\}_x$ and $\{N\}_y$ represent the partial derivative of the base functions in x and y coordinates.

The capacitances C and C_1 can be easily obtained from the microwave electric field. The simulations were performed for a guide built in an *x*-cut, *y*-propagating $LiNbO_3$ substrate, an isotropic buffer layer of SiO_2 and wavelength of 1.523 μm. The following parameters were assumed for the diffusion process, which determines the characteristics of the optical waveguide: initial width of Ti-strip W = 5 μm, initial thickness of Ti-strip H = 80 nm, diffusion temperature T = 1050°C and diffusion time t = 3 h [6], [10]-[12]. These parameters were chosen to guarantee the complete diffusion of Ti into the $LiNbO_3$ substrate and to produce a small optical spot size, in order to locate the optical waveguide where the electrooptic interaction is more intense.

The refractive indexes dispersion of the SiO_2 and of the $LiNbO_3$ was taken into account by using the three-terms Sellmeier equation for SiO_2 and the equivalent relations for $LiNbO_3$ presented in [8]. The electric optic field E_{op} is computed as presented in [6].

III. RESULTS

Two modulator configurations, named conventional and floating from this time on, are considered. In the conventional configuration, three symmetrical electrodes are deposited on a plane structure composed of a SiO_2 buffer layer on a $LiNbO_3$ substrate. The floating configuration includes three floating electrodes between the substrate and the buffer layer.

The geometric parameters used for the simulations presented in this work are: electrode width X = 50 μm, central electrode width S = 8 μm, electrode thickness e = 4 μm and gap between floating electrodes g' = 5 μm (for the floating configuration only). Very thin floating electrodes (zero thickness) were assumed.

The ratio R of the modulation electric field strength E_x for the floating configuration to the conventional one:

$$R(x,y) = \frac{E_x^{float}(x,y)}{E_x^{conv}(x,y)} \ , \tag{11}$$

and the contour lines, projected in the x-y plane, of the fundamental optical field strength in steps of 10% of the maximum optical electric field E_{op}, are shown in Fig. 2.

The ratio R and the optic-field normalized strength E_x along a vertical line which passes through the center of the optic-guide are presented in Fig. 3. Figs. 2 and 3 show clearly that the inclusion of floating electrodes results a remarkable increase of the modulator field strength in the region of maximum optic field. Thus, they increase the electrooptic interaction and reduce the power required for the operation of the modulator device, as pointed in [1].

Figs. 4 and 5 present the effective index (TEM wave) and the characteristic impedance of the conventional and floating configurations, respectively, as a function of the distance between the electrodes G and the buffer layer thickness b.

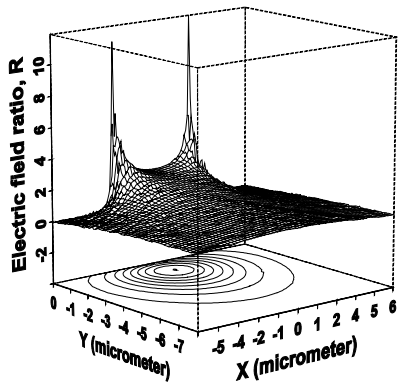

Fig. 2. *The ratio R of the modulation electric field strength E_x for the floating configuration to the conventional one. The contour lines on the x-y plane show the optic mode field distribution for the region of one of the optic guides.*

Fig. 6 presents the bandwidth variation as a function of G, for both conventional and floating configurations. The floating configuration modulator presents a greater bandwidth when compared with the conventional configuration for all gap dimensions. Fig. 7 presents the overlap integral factor Γ, and the half-wave voltage V_π as functions of the spacing dimension between floating electrodes g'. The increase of g' leads to a situation equivalent to that of a conventional layout, in other words, Γ becomes smaller and V_π grows up.

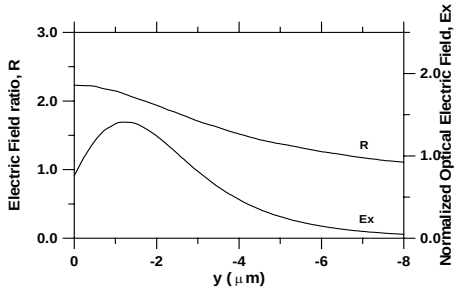

Fig. 3. *The ratio R of the modulation electric field strength E_x for the floating configuration to the conventional one and the normalized field strength for the fundamental optic mode along a vertical line which passes through the center of the gap.*

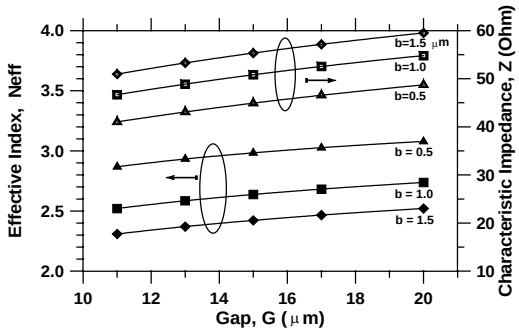

Fig. 4. *The variations of the characteristic impedance and of the effective index for a conventional configuration as a function of the distance between electrodes (gap) for various buffer layer thicknesses.*

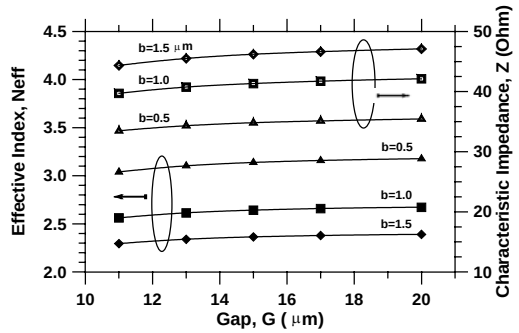

Fig. 5. *The variations of the characteristic impedance and of the effective index for a floating configuration as a function of the distance between electrodes (gap) for various buffer layer thicknesses.*

The electrical parameters of the conventional (A) and of the floating (B) configurations at the optimum electrical condition are compared in Table I. The geometrical parameters are: G = 15 μm and b = 1.5 μm. In both cases, the same Ti diffusion conditions are used. The numerical results show that the floating electrodes improve the performance of the device. A good impedance matching and larger bandwidth, 50% reduction in the half-wave voltage and a decrease of 75% in the driving power are obtained, when compared with the conventional configuration.

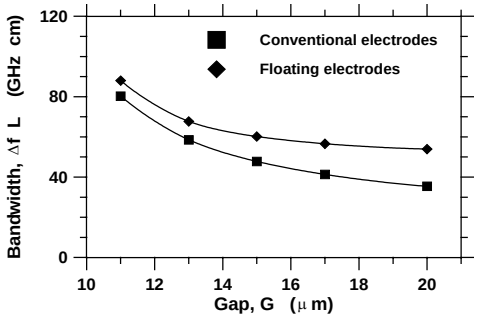

Fig. 6 *Bandwidth (Δf L) as a function of the distance between electrodes, G, for both conventional and floating configurations.*

TABLE I
ELECTRICAL PARAMETERS AT OPTIMIZED CONDITION. (A) CONVENTIONAL CONFIGURATION AND (B) FLOATING CONFIGURATION

CPW	Z (Ω)	N_{eff}	$\Delta f\ L$ (GHz cm)	$\lvert\Gamma\rvert$	$V_\pi L$ (V cm)	$P_{in} L^2$ (W cm^2)
A	55.33	2.422	47.76	0.230	16.446	0.678
B	46.20	2.364	60.16	0.463	8.193	0.168

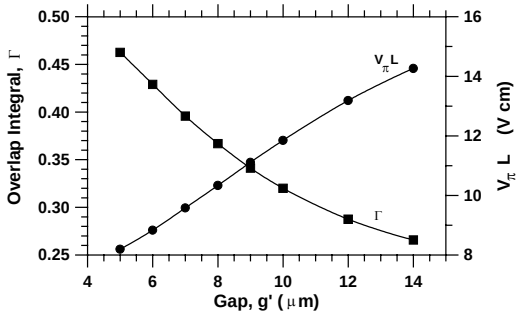

Fig. 7. *The overlap integral factor and the half-wave voltage as functions of the gap dimension g' between the floating electrodes.*

CONCLUSIONS

A *x*-cut Ti:$LiNbO_3$ traveling-wave optical modulator with extra floating electrodes was analyzed by applying the finite element method. The floating configuration allows the reduction of the effective index, the increase of the bandwidth, and the reduction of power consumption with respect to the conventional configuration. The numerical results complement information presented previously in literature. They allow the evaluation of relevant physical parameters of the optical modulators in terms of geometric dimensions of the CPW transmission lines.

REFERENCES

[1] S. Hopfer, Y. Shani and D. Nir, "A Novel, Wideband, Lithium Niobate Electrooptic Modulator," *IEEE J. Lightwave Technol.*, vol. 16, No. 1, pp. 73-77, 1998.

[2] K. Kawano, "High-Speed Shielded Velocity-Matched Ti:$LiNbO_3$ Optical Modulator," *IEEE J. Quantum Electron.*, vol. 29, No.9, pp. 2466-2475, 1993.

[3] X. Zhang and T. Miyoshi, "Optimum Design of Coplanar Waveguide for $LiNbO_3$ Optical Modulator,"

IEEE Trans. Microwave Theory Tech., vol. 43, No.3, pp. 523-528, 1995.

[4] H. Chung, W. S. C. Chang, and E. L. Adler, "Modeling and Optimization of Traveling-Wave $LiNbO_3$ Interferometric Modulators," *IEEE J. Quantum Electron.*, vol.27, No. 3, pp. 608-617, 1991.

[5] K. W. Hui, K. S. Chiang, B. Wu, and Z. H. Zhang, "Electrode Optimization for High-Speed Traveling-Wave Integrated Optic Modulators," *J. Lightwave Technol.*, vol. 16, No.2, pp.232-238, 1998.

[6] M. A. R. Franco, A. Passaro, J. R. Cardoso, and J. M. Machado, "Finite Element Analysis of Anisotropic Optical Waveguide with Arbitrary Index Profile," *IEEE Trans. Magn.*, vol.35, No.3, pp. 1546-1549, 1999.

[7] M. A. R. Franco, A. Passaro, F. Sircilli Neto, J. R. Cardoso, and J. M. Machado, "Modal Analysis of Anisotropic Diffused-Channel Waveguide by a Scalar Finite Element Method," *IEEE Trans. Magn.*, vol. 34, No. 5, pp.2783-2786, 1998.

[8] M. Koshiba, *Optical Waveguide Theory by the Finite Element Method*, 1st ed., KTK Scientific Publishers, Tokyo, 1992, pp. 126, 219-220.

[9] H. Nishihara, M. Haruna, and T. Suhara, *Optical Integrated Circuits*, 1st ed., McGraw-Hill, 1989, pp.109-111.

[10] D. Zhang, C. Chen, J. Li, G. Ding, X. Chen, and Y. Cui, "A Theoretical Study of a Ti-Diffused Er:$LiNbO_3$ Waveguide Laser," *IEEE J. Quantum Electron.*, vol. 32, N. 10, pp. 1833-1838, 1996.

[11] D. Zhang, C. Chen, G. Ding, J. Zhang, and Y. Cui, "Dependence of Ti-Diffused Er:$LiNbO_3$ Laser Efficiency on Waveguide Fabrication Parameters and Pump Wavelength," *IEEE J. Quantum Electron.*, vol. 33, No. 7, pp. 1231-1235, 1997.

[12] S. Fouchet, A. Carenco, C. Daguet, R. Guglielmi, and L. Riviere, "Wavelength Dispersion of Ti Induced Refractive Index Change in $LiNbO_3$ as a Function of Diffusion Parameters," *J. Lightwave Technol.*, vol. LT-5, N. 5, pp. 700-708, 1987.

Marcos Antonio Ruggieri Franco was graduated in Physics at Pontifícia Universidade Católica de São Paulo – Brazil (PUC-SP), in 1983. In 1991, he finished his Master of Science degree in Nuclear Physics at Instituto de Física da Universidade de São Paulo-Braxil (IFUSP). In 1999, he received his doctorate in Electrical Engineering from the Escola Politécnica da Universidade de São Paulo – Brazil (POLI-USP). In 1987, he joined the research team of the division of Applied Physics at Institute for Advanced Studies (IEAv) at Centro Técnico Aeroespacial (CTA). Since 2001, he is also associated professor of the pos-graduate course of Electronic Computation Engineering from the Instituto Tecnológico de Aeronáutica (ITA). His major areas of interest are the application of the Finite Element Method for the design of electromagnetic devices sucha as microwave and optical waveguides, fiber optics, integrated optics, antennas and electromagnetic scattering problems.
(email: marcos@ieav.cta.br)

Angelo Passaro received the B.Sc. in physics (1981) and the M.Sc degrees in nuclear physics (1988) from the Instituto de Física da Universidade de São Paulo (IFUSP), Brazil. In 1998, he completed his doctorate degree in electrical engineering at the Escola Politécnica da Universidade de São Paulo (EPUSP), Brazil. In 1984, he joined the Institute for Advanced Studies of Aerospace Technical Center. Since 1999, he has been the head of the Virtual Engineering Laboratory of (IEAv-CTA). His current research interests are in high-performance parallel programming, numerical methods, electromagnetic field computation, plasma simulation, and heat conduction analysis.
(email: angelo@ieav.cta.br)

Nancy Mieko Abe obtained the B.Sc. and M.Sc. degrees in electrical engineering from the Escola Politécnica da Universidade de São Paulo (EPUSP), Brazil, in 1989 and 1992, respectively. In 1997, she obtained the doctorate degree in electrical engineering from the same university (EPUSP). In 1998, she joined the Institute for Advanced Studies of Aerospace Technical Center (IEAv-CTA), Brazil, as a researcher fellow. Since 2002 she is an Adjunct Researcher in the Virtual Engineering Laboratory of IEAv/CTA. Her research interests include electromagnetic field computation, heat conduction analysis, plasma simulation, numerical methods and high-performance parallel programming.
(email: nancy@ieav.cta.br)

José Marcio Machado obtained his Doctorate in Electrical Engineering from the Escola Politécnica da Universidade de São Paulo (1993). In 1985, he finished his Master of Science at the Centro Brasileiro de Pesquisas Físicas (CBPF). Nowadays, he is a professor of Mathematics at the Universidade do Estado de São Paulo – Brazil (UNESP-São José do Rio Preto) at Computation Science. His major researches interests are numerical methods, differential equations and applications for Physics, Mathematics and Engineering.
(email: jmarcio@dcce.ibilce.unesp.br)

Francisco Sircilli Neto was graduated at the Institute of Physics of São Paulo University (IFUSP), Brazil, in 1981. His Master of Science was obtained in 1986 at the National Institute for Space Research (INPE), Brazil, in the area of Nuclear Geophysics. In 1997 he concluded his Doctorate in Electrical Engineering at the Polytechnic School of São Paulo University (POLI-USP), Brazil. Since 1985 he joined the research team of Division of Applied Physics of the Institute for Advanced Studies of the Aerospace Technical Center (IEAv/CTA). Today his main area of interest is the application of the Finite Element Method (FEM) to wave propagation in devices such as microwave, optical waveguides and fiber optics, as well as to antennas and electromagnetic scattering problems.
(email:sircilli@ieav.cta.br)

Treinamento Corporativo

CANAL.

Programas de Treinamento Corporativo no Instituto que oferece o estado-da-arte em pesquisa e avanços tecnológicos.

As maiores companhias do país contratam os Programas de Treinamento Corporativo do Inatel Competence Center. O Inatel detecta as necessidades de treinamento, desenvolve o programa adequado, considerando o potencial dos colaboradores e os objetivos da empresa, além de avaliar o conhecimento adquirido em cada um dos cursos e os benefícios do Treinamento. O ICC também atua na área de terceirização de treinamento, em regime total ou parcial.

Categorias

- Comunicações Via Satélite
- Gestão em Telecomunicações
- Redes de Computadores
- Sistemas de Telecomunicações
- Sistemas Celulares
- Sistemas de Computação
- Sistemas de Dist. de sinais de TV
- Testes e Medidas em Telecom.

Mais de 700 profissionais de 80 empresas optaram por especialistas em constante atualização do Inatel.

Consulte nossa programação de cursos abertos em
www.inatel.br/treinamento

Inatel
COMPETENCE CENTER

Pós-Graduação Lato Sensu

Os objetivos da empresa
e da sua carreira aliados à
competência e ao nível de
desenvolvimento do Inatel.

Pós-graduação no Instituto que oferece o estado-da-arte em pesquisa no Brasil.

Cursos de Pós-Graduação do Inatel:*

Engenharia de Sistemas de TV Digital
Engenharia de Redes e Sistemas de Telecomunicações

Para empresas e profissionais interessados em se atualizar e conhecer os maiores avanços e pesquisas em telecomunicações e tecnologia da Informação, satisfazendo os requisitos do competitivo mercado de trabalho.
Mais de 80 empresas de telecomunicações e TI já aprovaram nossos programas.

Turmas em
São Paulo,
Campinas,
Brasília e
Belo Horizonte

Inscrições abertas - www.inatel.br/pos
Tel. (35) 3471.9350 - e-mail: pos@inatel.br

Instituto Nacional de Telecomunicações
Av. João de Camargo, 510 - Santa Rita do Sapucaí, MG - CEP 37540-000

Inatel
COMPETENCE CENTER

PROJETO EDITORIAL

A revista *Telecomunicações* tem por objetivo oferecer aos profissionais que atuam no segmento das telecomunicações uma obra de caráter técnico-científico de divulgação dos trabalhos de desenvolvimento e pesquisa, realizados no Brasil e em outros países.

A revista *Telecomunicações* aceita artigos inéditos, não publicados e que não estejam submetidos a outra publicação, nas seguintes modalidades: tutorial, científico e de engenharia aplicada. Os artigos podem ter conteúdo científico ou voltado para a solução de problemas de engenharia nos diversos segmentos das telecomunicações e podem ser redigidos em português ou inglês. A revista possui duas edições anuais, com tiragem de 5.300 exemplares em cada edição, distribuídas entre os profissionais atuantes no setor.

O Corpo Editorial da revista *Telecomunicações* é formado por renomados pesquisadores de diversas instituições de ensino e pesquisa do Brasil e do exterior. Os artigos submetidos são avaliados pelos membros do Corpo Editorial ou por especialistas designados por estes. Os resultados da avaliação indicarão a aceitação ou rejeição do artigo e serão encaminhados para os autores em formulário padrão (disponível em www.inatel.br/revista). Os itens avaliados são: atualidade do tema, aplicabilidade dos resultados, originalidade dos resultados ou da abordagem, clareza do texto, referências bibliográficas e profundidade. O peso de cada item depende da natureza do artigo submetido. Almeja-se que o intervalo de tempo entre a submissão do artigo e o envio da resposta aos autores não ultrapasse 60 dias.

INSTRUÇÕES PARA OS AUTORES

Submetendo Artigos para Publicação

Os artigos devem ser encaminhados, em formato pdf, para o e-mail submission@inatel.br. O formato para a 1ª submissão é em coluna única, espaçamento duplo, fonte Times New Roman 12, com no máximo 40 páginas em tamanho A4. O artigo deve conter o nome de todos os autores e o endereço completo (endereço postal, telefone, fax, e-mail) de pelo menos um dos autores.

Versão Final do Artigo

O formato final para o envio de artigos aceitos para publicação é o definido no modelo disponível na página www.inatel.br/revista. Sombras e cores devem ser evitadas a fim de facilitar o processo

O MERCADO TEM PERGUNTAS. TELEXPO, AS RESPOSTAS.

Congresso Telexpo 2005

A Telexpo 2005 assume o papel de evento chave para os mercados e tecnologias de comunicações e informações visando a melhoria da capacitação dos profissionais e a competitividade das suas empresas, tanto fornecedoras quanto usuárias dos produtos e serviços do setor, estimulando a geração e crescimento das linhas de negócios das suas cadeias produtivas e criando um ambiente propício à discussão das ações de governo e da sociedade no rumo do desenvolvimento tecnológico do país.

35 painéis de atualização mercadológica em **9** fóruns que abordarão as aplicações, soluções, produtos e tecnologias mais adequados aos negócios

- Aplicações e Inteligência das Informações
- Contexto e Políticas Tecnológicas
- Convergência de Redes e Serviços
- Dimensão da Gestão das Informações
- Infra-estrutura e Gestão de Redes
- Integração, Segurança e Qualidade dos Serviços
- Contact Center
- VoIP e Telefonia IP
- Wireless e Internet

Participe do principal Congresso de Telecomunicações e Tecnologia da Informação

TELEXPO 2005

Telecomunicações e Tecnologia da Informação
Onde os Negocios Acontecem

01 a 04 de março de 2005

Expo Center Norte

São Paulo - Brasil

Informações:

11 3040.7899

telexpo@advanstar.com.br

www.telexpo.com.br

Apoio Institucional:

ANATEL — Ministério do Desenvolvimento, Indústria e Comércio Exterior — BRASIL UM PAÍS DE TODOS GOVERNO FEDERAL — abinee

Revista Oficial: RNT — Revista de Negócios em Telecomunicações — O Mercado ao seu Alcance

Um evento: ADVANSTAR EDITORA E COMUNICAÇÕES